Monthly Notices
of the
ROYAL ASTRONOMICAL SOCIETY

MNRAS **475,** 404–423 (2018)
Advance Access publication 2017 December 8

doi:10.1093/mnras/stx3161

The relativistic jet of the γ-ray emitting narrow-line Seyfert 1 galaxy 1H 0323+342

Daniel Kynoch,[1]★ Hermine Landt,[1] Martin J. Ward,[1] Chris Done,[1] Emma Gardner,[1] Catherine Boisson,[2] Maialen Arrieta-Lobo,[2] Andreas Zech,[2] Katrien Steenbrugge[2,3] and Miguel Pereira Santaella[4]

[1]*Centre for Extragalactic Astronomy, Department of Physics, Durham University, South Road, Durham, DH1 3LE, UK*
[2]*LUTH, Observatoire de Paris, CNRS, Université Paris Diderot, PSL Research University Paris, 5 place Jules Janssen, F-92195 Meudon, France*
[3]*Instituto de Astronomía, Universidad Católica del Norte, Avenida Angamos 0610, Antofagasta, Chile*
[4]*Department of Physics, University of Oxford, Keble Road, Oxford, OX1 3RH, UK*

Accepted 2017 December 4. Received 2017 December 4; in original form 2017 August 23

ABSTRACT

The detection of several radio-loud narrow-line Seyfert 1 (NLS1) galaxies by the *Fermi Gamma-Ray Space Telescope* hints at the existence of a rare, new class of γ-ray emitting active galactic nuclei with low black hole masses. Like flat spectrum radio quasars (FSRQs), their γ-ray emission is thought to be produced via the external Compton mechanism whereby relativistic jet electrons upscatter a photon field external to the jet, e.g. from the accretion disc, broad line region (BLR), and dusty torus, to higher energies. Here we study the origin of the γ-ray emission in the lowest-redshift candidate among the currently known γ-ray emitting NLS1s, 1H 0323+342, and take a new approach. We observationally constrain the external photon field using quasi-simultaneous near-infrared, optical, and X-ray spectroscopy. Applying a one-zone leptonic jet model, we simulate the range of jet parameters for which this photon field, when Compton scattered to higher energies, can explain the γ-ray emission. We find that the site of the γ-ray emission lies well within the BLR and that the seed photons mainly originate from the accretion disc. The jet power that we determine, 1.0×10^{45} erg s^{-1}, is approximately half the accretion disc luminosity. We show that this object is not simply a low-mass FSRQ, its jet is intrinsically less powerful than predicted by scaling a typical FSRQ jet by black hole mass and accretion rate. That γ-ray-emitting NLS1s appear to host underpowered jets may go some way to explaining why so few have been detected to date.

Key words: galaxies: active – galaxies: individual: 1H 0323+342 – galaxies: jets – galaxies: Seyfert – gamma-rays: galaxies.

1 INTRODUCTION

The detection of several narrow-line Seyfert 1 (NLS1) galaxies by the *Fermi Gamma-Ray Space Telescope* suggests the existence of a rare, new class of γ-ray emitting active galactic nuclei (AGNs). These are similar to the standard blazars in that their *Fermi* γ-ray emission is dominated by a relativistic jet aligned close to the line of sight, but distinctly different in that this is powered by accretion on to a black hole (BH) of much lower mass (Abdo et al. 2009b; Foschini 2011). The mechanisms by which such relativisitic jets are launched and accelerated remain poorly understood. These γ-NLS1s can provide new insights on how these processes might scale with BH mass.

★E-mail: daniel.kynoch@durham.ac.uk

Fermi-detected blazars can be divided into two types: BL Lacertae objects (BL Lacs) and flat spectrum radio quasars (FSRQs). These can be distinguished by their broad-band spectral energy distributions (SEDs). The BL Lac SEDs show two broad humps of emission that are roughly equal in luminosity. One hump arises from synchrotron processes (generally peaking in the radio/infrared (IR)/optical) and the other from the synchrotron self-Compton mechanism (generally peaking in the GeV range) from the same population of highly relativisitic electrons (with Lorentz factors of up to $\gamma \sim 10^{5-6}$) accelerated within the jet. The entire SED is dominated by this emission, boosted along the line of sight by the relativisitic bulk Lorentz factor ($\Gamma_{\rm BLF} \sim 10$–20) of the jet. In contrast, the FSRQs have GeV Compton humps that are considerably more luminous than their synchrotron emission humps, and they additionally show a clear accretion disc spectrum as a third hump in the region between the two jet emission components, together with

an associated broad line region (BLR). These differences can be understood in the context of a change in the nature of the accretion flow, with the BL Lacs having low accretion rates so the accretion flow is in the hot, advection-dominated state with little intrinsic ultraviolet (UV) emission and hence a very weak or absent BLR. These advection-dominated accretion flows (ADAFs) collapse into a standard disc at luminosities above a few per cent of the Eddington luminosity, so the higher luminosity FSRQs have a UV bright disc which provides the ionization to produce a BLR, which in turn gives an additional source of seed photons external to the jet for Comptonization (external Compton: EC), leading to the observed much brighter Compton hump (Ghisellini, Maraschi & Tavecchio 2009). The BH mass can be derived from standard BLR scaling relations for the FSRQs, and is always found to be very high, with $M_{\rm BH} \gtrsim 10^8$ M$_\odot$ (e.g. Ghisellini & Tavecchio 2015). Conversely, it is much more difficult to constrain in BL Lacs as these have very weak (or no) lines, but studies of the host galaxies conclude that these are powered by similarly high mass BHs (e.g. Falomo et al. 2003; Plotkin et al. 2011). Together the BL Lacs and FSRQs form a standard 'blazar sequence' of increasing accretion power on to the most massive BHs (Fossati et al. 1998; Ghisellini et al. 2017). In terms of AGN unification schemes, it is insightful to investigate whether γ-NLS1s represent the low-mass, low-power tail of FSRQs in this sequence or whether they constitute a genuinely new class of their own.

At larger inclination angles Doppler de-boosting means that the jet does not dominate the SED but these objects are still easily identified by their strong radio emission from both the jet core and large-scale radio lobes. This is often quantified as a radio-loudness parameter, defined from a radio-to-optical flux ratio $R = f_{5\,\rm GHz}/f_{B\,\rm band}$, with $R > 10$ defining a radio-loud (RL) quasar. Radio-quiet (RQ) quasars and the lower-power Seyfert AGN can exhibit radio jet structures, but these are slow, and poorly collimated compared with blazar jets (e.g. Middelberg et al. 2004).

Early studies (e.g. Laor 2000; McLure & Dunlop 2001) found no evidence of an RL-AGN population with BH masses $M_{\rm BH} \lesssim 10^8$ M$_\odot$. High-mass BHs are almost exclusively found in elliptical galaxies with large bulges, leading to ideas that there is something about the evolutionary history of these systems which triggers jet production such as BH spin (Blandford & Znajek 1977) or the history of concentration of magentic flux (Sikora & Begelman 2013) or both. However, this simple paradigm is now being challenged by the discovery of lower-mass RL-AGNs (Ho 2002; Yuan et al. 2008) which are instead hosted by spiral galaxies. A few of these have been detected by *Fermi*, and appear to form a low-mass, low-power tail of the FSRQ population, with a detectable disc component and BLR, together with dominant EC emission. The BLR line velocity widths are fairly narrow, often with FWHM below 2000 km s^{-1}, which forms the (arbitrary) cut-off for an object designated as a NLS1 (Osterbrock & Pogge 1985). Such low velocities of the BLR gas indicate a low-mass BH accreting at a high Eddington fraction. The percentage of NLS1s that are RL (≈7 per cent, Komossa et al. 2006; and ≈5 per cent, Rakshit et al. 2017) is low when compared with the RL fraction of AGN generally (≈15 per cent), but a few (currently 10) of the RL-NLS1s have now been detected by *Fermi* as γ-NLS1s (Abdo et al. 2009a,b; Donato & Perkins 2011; Calderone et al. 2012; D'Ammando et al. 2015; Yao et al. 2015b; D'Ammando et al. 2016), confirming the presence of powerful, relativistic jets in these sources.

Whilst jet emission processes are relatively well-understood, the mechanisms by which jets are launched and powered are still areas of intense research. Ghisellini et al. (2014) found a clear correlation between jet powers and accretion disc luminosities, but with the jet power exceeding the disc luminosity typically by a factor of 10. The jet launching mechanism must therefore be very efficient and in some way linked to the accretion flow. The γ-NLS1s are ideal objects to investigate this disc–jet connection, since they are nearby ($z < 1$), very high accretion rate objects with luminous discs and blazar-like jets.

Here, we present a detailed study of the nearest γ-NLS1, 1H 0323+342[1] (RA: 03 24 41.16, Dec: +34 10 45.8), at a redshift of $z = 0.0625$ (Landt et al. 2017). High-energy γ-ray emission has been associated with its radio counterpart with high significance and was first reported by Abdo et al. (2009b). In this paper we assemble an unprecedentedly well-sampled SED containing several relatively high signal-to-noise ratio (S/N) spectra as well as complementary photometry. SEDs for this object have previously been presented in e.g. Abdo et al. (2009b), Paliya et al. (2014), and Yao et al. (2015a), but here we include much more spectral and photometric data to assemble a more detailed and quasi-simultaneous SED. Our new approach is to use this SED to self-consistently determine the seed photons available for the EC component, so we are able to better incorporate the differences between the BLR size scale between this and the more massive FSRQs.

This paper is organized as follows. In Section 2 we present the multiwavelength data set we have assembled for this source, and in Section 3 we provide a detailed analysis of the *XMM–Newton* X-ray spectrum. We describe how we use these data to determine the ambient photon field contributions from the accretion disc, X-ray corona, BLR, and torus in Section 4.1. In Section 4.2 we use a jet emission code to compute the radiative output resulting from the jet's interaction with this photon field and attempt to recover the jet parameters which best describe the broad-band SED. The discussion and conclusions are presented in Sections 5 and 6, respectively. Throughout this paper, we assume a ΛCDM (cold dark matter) cosmology with $H_0 = 70$ km s^{-1} Mpc^{-1}, $\Omega_{\rm m} = 0.3$ and $\Omega_\Lambda = 0.7$. Therefore the redshift $z = 0.0625$ implies a luminosity distance of 280 Mpc and a flux-to-luminosity conversion factor of 9.41×10^{54} cm^2.

2 THE MULTIWAVELENGTH DATA SET

Below we present the multiwavelength data set we have assembled for 1H 0323+342. As a whole this data set is non-simultaneous, however parts of it are quasi-simultaneous. In particular, the observations which we use to calculate the external photon field (including near-IR, optical, and X-ray spectroscopy; see Section 4.1) were all obtained in a time span of less than 6 months. The issue of variability is addressed in Sections 3.1 and 5.4 and is the subject of a forthcoming paper (Arrieta-Lobo et al., in preparation). The data set spans an exceptionally wide range of frequencies, from ∼10^9 Hz in the radio up to ∼10^{24} Hz in γ-rays. In addition, the SED is also well-sampled, with data in the radio, IR, optical, UV, X-rays, and γ-rays. Because it is a bright source, many of these data are high S/N and include spectra in the IR, optical, and X-ray as well as photometry. Here, we present our new reductions/extractions of data from the *Spitzer Space Telescope* (Section 2.2.1); *XMM–Newton* (Section 2.1.3), and *Fermi* (Section 2.3.3). We also summarize the data which were used previously by Landt et al. (2017). These data sets are supplemented by archival data from other facilities in the radio/sub-mm, IR, UV, and X-ray bands. The complete data set and

[1] The J2000 name of this source, J0324+3410, is used in some other papers.

Table 1. The multiwavelength data set.

Q	Band	Instrument (survey)	Observation date (D/M/Y or M/Y)	log (ν_{obs}) (Hz)	Flux (10^{-14} erg s^{-1} cm^{-2})	Luminosity (10^{41} erg s^{-1})	Ref.
	Radio	Effelsberg	07/10–03/14	9.422	1.22 ± 0.16	1.15 ± 0.15	[1]
	Radio	Effelsberg	07/10–03/14	9.686	1.94 ± 0.31	1.82 ± 0.29	[1]
	Radio	Effelsberg	07/10–03/14	9.922	3.17 ± 0.64	2.98 ± 0.60	[1]
	Radio	Effelsberg	07/10–03/14	10.02	3.94 ± 0.87	3.71 ± 0.82	[1]
	Radio	Effelsberg	07/10–03/14	10.16	5.5 ± 1.7	5.2 ± 1.5	[1]
	Radio	Effelsberg	07/10–03/14	10.36	11.5 ± 5.3	10.8 ± 5.0	[1]
	Radio	Effelsberg	07/10–03/14	10.51	13.8 ± 8.7	13.0 ± 8.2	[1]
	Radio	Effelsberg	07/10–03/14	10.63	15.2 ± 5.0	14.3 ± 4.7	[1]
	Radio	IRAM	07/10–03/14	10.94	47 ± 1.5	43.9 ± 1.4	[1]
	Radio	*Planck*	08/09–11/10	11.00	56.4 ± 5.2	53.1 ± 4.9	[2]
	Radio	IRAM	07/10–03/14	11.15	73.7 ± 2.3	69.3 ± 2.2	[1]
	Radio	*Planck*	08/09–11/10	11.16	93.8 ± 5.7	88.2 ± 5.4	[2]
	Radio	*Planck*	08/09–11/10	11.34	89.3 ± 9.4	84.0 ± 0.9	[2]
	Far-IR	*Spitzer* MIPS	27/09/08	12.63	869 ± 8	817 ± 8	[3]
	Far-IR	*WISE*	10–11/02/10	13.13	1400 ± 70	1320 ± 70	[4]
	Far-IR	*Spitzer* IRS[a]	27/09/08	13.30	1130 ± 140	1060 ± 130	[3]
	Mid-IR	*WISE*	10–11/02/10	13.41	1360 ± 70	1280 ± 70	[4]
	Mid-IR	*Spitzer* IRAC	27/09/08	13.58	1390 ± 70	1310 ± 70	[3]
	Mid-IR	*Spitzer* IRAC	27/09/08	13.72	1230 ± 60	1160 ± 60	[3]
	Mid-IR	*WISE*	10/02/10–20/08/10	13.81	1150 ± 50	1080 ± 50	[4]
	Mid-IR	*Spitzer* IRAC	27/09/08	13.82	1230 ± 60	1150 ± 60	[3]
	Mid-IR	*Spitzer* IRAC	27/09/08	13.92	1260 ± 60	1180 ± 60	[3]
	Mid-IR	*WISE*	10/02/10–20/08/10	13.95	1310 ± 80	1230 ± 80	[4]
	Near-IR	(2MASS)	20/01/98	14.14	1170 ± 30	1100 ± 30	[5]
✓	Near-IR	GNIRS[a]	16/09/15	14.25	1030 ± 50	970 ± 50	[6]
	Near-IR	(2MASS)	20/01/98	14.26	1100 ± 40	1030 ± 40	[5]
	Near-IR	(2MASS)	20/01/98	14.39	1040 ± 30	980 ± 30	[5]
✓	Optical	Keck[a]	14/02/16	14.65	950 ± 50	890 ± 50	[6]
✓	Optical	*XMM–Newton* OM	23/08/15	14.74	1990 ± 10	1872 ± 9	[3]
✓	Optical	*XMM–Newton* OM	23/08/15	14.82	1856 ± 8	1746 ± 8	[3]
✓	UV	*XMM–Newton* OM	23/08/15	14.94	1963 ± 8	1847 ± 8	[3]
✓	UV	*XMM–Newton* OM	23/08/15	15.01	2600 ± 10	2446 ± 9	[3]
	UV	*GALEX*	27/12/11	15.11	2800 ± 1000	2600 ± 900	[7]
✓	UV	*XMM–Newton* OM	23/08/15	15.11	3010 ± 30	2830 ± 30	[3]
✓	UV	*XMM–Newton* OM	23/08/15	15.15	3190 ± 50	3000 ± 50	[3]
✓	X-ray	*XMM–Newton* EPIC[a]	23/08/15	17.68	430 ± 10	400 ± 10	[3]
	X-ray	*NuSTAR*[a]	15–18/03/14	18.67	720 ± 20	680 ± 20	[6]
	X-ray	*Swift* BAT[a]	12/04–09/10	19.18	995 ± 200	940 ± 200	[8]
	γ-ray	*Fermi* LAT	01/08/15–30/09/15	22.39	1500 ± 450	1400 ± 420	[3]
	γ-ray	*Fermi* LAT	01/08/15–30/09/15	23.00	370 ± 130	345 ± 120	[3]
	γ-ray	*Fermi* LAT	01/08/15–30/09/15	23.74	70 ± 50	65 ± 50	[3]

Notes. [a]For spectra, we quote the flux at the indicated frequency at approximately the midpoint of each spectrum. The 'Q' flag indicates the quasi-simultaneous data from which we determine the external seed photon field, as described in Section 4.1 in the text. References: [1] Angelakis et al. (2015); [2] *Planck* Second Point Source Catalog, Planck Collaboration XXVI (2016); [3] this work; [4] *WISE* AllWISE Source Catalog, Wright et al. (2010); [5] Two Micron All-Sky Survey, Skrutskie et al. (2006); [6] Landt et al. (2017); [7] *GALEX* Data Release GR6, Martin et al. (2005); [8] *Swift* BAT 70-month All-Sky Hard X-ray Survey, Baumgartner et al. (2013).

its reference sources are listed in Table 1. The multiwavelength SED is shown in Fig. 1.

2.1 Quasi-simultaneous data sampling the external photon field

Although not strictly simultaneous, we have obtained three spectra (in the IR, optical, and X-ray bands) and optical/UV photometry sampling the accretion flow which were taken over a period of less than 6 months. In Section 4.1.1, we use these quasi-simultaneous data to parametrize the size scales and luminosities of the accretion disc, its X-ray corona, and the hot dust emission from the torus, which (along with the BLR) contribute to the external photon field which is Compton upscattered by particles in the relativistic jet. In Section 2.3.3 we extract *Fermi* γ-ray emission spanning a period from approximately a month either side of the *XMM–Newton* observation.

2.1.1 Gemini North

The near-IR spectrum, obtained in 2015 September using the Gemini Near-Infrared Spectrograph (GNIRS) on the Gemini North 8 m telescope, was presented in Landt et al. (2017). The average continuum S/N obtained in the *J*, *H*, and *K* bands were ∼40, 70, and 90, respectively. The spectrum was dereddened using the calculated extinction value $A_V = 0.71$ from the Galactic neutral hydrogen column density $N_H = 1.46 \times 10^{21}$ cm^{-2} given by Dickey & Lockman (1990, hereafter D&L90).

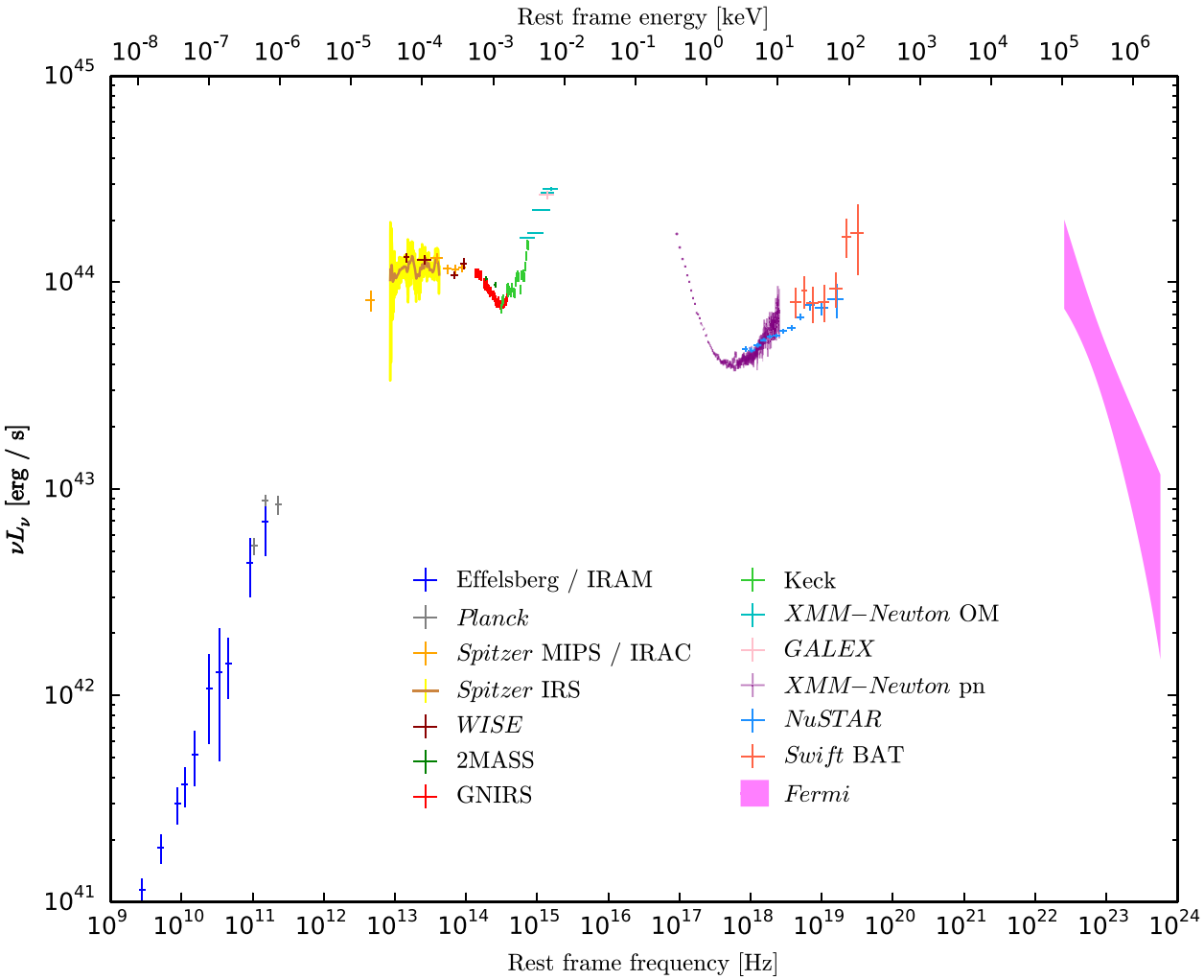

Figure 1. The multiwavelength SED of the γ-NLS1 1H 0323+342. The *XMM-Newton* X-ray spectrum has been deabsorbed using a Galactic column $N_{\rm H}^{\rm Gal} = 2.3 \times 10^{21}$ cm^{-2}. The optical / UV data have been dereddened using an $A_V = 0.71$. For details of the original sources of these multiwavelength data, see Table 1.

2.1.2 *Keck*

The optical spectrum was obtained using the Low Resolution Imaging Spectrometer mounted on the Keck 10 m telescope in 2016 February. As described in Landt et al. (2017), the average continuum S/N was ∼60 and we scaled up this spectrum in flux by ≈40 per cent to match the near-IR spectrum.

2.1.3 *XMM–Newton*

The large effective area of the *XMM–Newton* X-ray observatory (Jansen et al. 2001) makes it an excellent telescope with which to obtain high S/N X-ray spectra. It carries three European Photon Imaging Camera (EPIC) detectors and a reflection grating spectrometer (RGS) which simultaneously conduct X-ray imaging and spectroscopy. Its optical monitor (OM) operates concurrently with the X-ray detectors and can cycle through six filters covering optical/UV wavelengths. 1H 0323+342 was observed by *XMM–Newton* for 81 ks on 2015 August 23–24. The three EPIC X-ray detectors (pn, MOS1, and MOS2) were operating in a Large Window mode with the Medium filter in place. Data from the observation (ID 0764670101; PI: D'Ammando) were obtained from the *XMM–Newton* Science Archive and the reduction was performed using the Science Analysis System (SAS, v15.0.0).

We extracted *XMM–Newton* OM photometry taken through all six filters using the SAS OMICHAIN and OMSOURCE tasks and standard procedures. Fluxes were calculated from the count rates in each filter and dereddened using our derived $A_{\rm V} = 0.71$ and adopting $R_{\rm V} = 3.1$ and the reddening correction curves of Cardelli, Clayton & Mathis (1989). Data and response files for use in the spectral fitting package XSPEC (Arnaud 1996) were generated using the FLX2XSP tool. Photometry from the *V* filter was excluded from our later analysis because it contains a strong emission line.

After filtering the EPIC event lists for flaring particle background, we were left with good exposure times of 60, 72, and 70 ks for the pn, MOS1, and MOS2 detectors, respectively. Source spectra from all three detectors were extracted from a 20-arcsec-radius circular region centred on the source. Background spectra were extracted from circular regions (60 arcsec radius for pn and 40 arcsec for MOS) on an offset blank patch of sky on the same chip as the source. Source count rates were 3.6, 0.94, and 1.0 counts s^{-1} in the pn, MOS1, and MOS2 detectors, respectively. The rate in pn exceeds the maximum rate of 1.5 counts s^{-1} for the avoidance of pile-up suggested in the Users Handbook. A test for pile-up was performed

Table 2. Summary of *XMM–Newton* exposures.

Detector	Energy (keV)	Live time (ks)	Counts
EPIC-pn	0.3–10	60	217 650
	0.33–2.5		182 664
EPIC-MOS1	0.3–10	72	68 017
	0.33–2.5		54 272
EPIC-MOS2	0.3–10	70	73 838
	0.33–2.5		58 693
RGS1	0.33–2.5	80	8912
RGS2	0.33–2.5	80	10 563

using the SAS EPATPLOT task and no evidence for pile-up was found. The extracted spectra were rebinned using the specgroup tool to achieve a minimum S/N of 5 in each group and not to oversample the intrinsic instrumental energy resolution by a factor greater than 3. Because of the large number of counts in the spectra, this easily satisfied the requirement for a minimum of 20 counts per bin needed for χ^2 analysis. Our detailed X-ray spectral and temporal analyses are presented in Section 3.

We also obtained the Pipeline Processing System (PPS) products from the two RGS instruments aboard *XMM–Newton*. These instruments cover the 0.33–2.5 keV range at a much higher spectral resolution than the EPIC CCDs. In our analysis we used only the first spectral orders (containing ∼20 000 counts in total; see Table 2).

2.2 Additional data sampling the external photon field

We supplement the data above with an IR spectrum and photometry from *Spitzer* which we attribute primarily to emission from the dusty torus (see Sections 2.2.1 and 5). Additionally, we have photometry from *WISE*, the 2MASS survey and *GALEX* in the same frequency ranges as the *Spitzer*, GNIRS and *XMM–Newton* OM data, respectively.

2.2.1 Spitzer

The *Spitzer Space Telescope* (Werner et al. 2004) carries three scientific instruments. Its Infrared Array Camera (IRAC) images simultaneously at the wavelengths 3.6, 4.5, 5.8 and 8 μm; the Infrared Spectrograph (IRS) covers the wavelength range between ≈5 and 40 μm; the Multiband Imaging Photometer (MIPS) contains three arrays operating at 24, 70 and 160 μm.

To obtain photometry from IRAC, we analysed the post-BCD (Basic Calibrated Data) images of 1H 0323+342 taken on the 2008 September 27 observation, available from the *Spitzer* archive. Using a 10 arcsec aperture, we determined fluxes at each of the four operating wavelengths with uncertainties ≈5 per cent.

The source was observed with IRS using the low spectral resolution ($R \sim 60$–130) modules between 7.6 and 37.9 μm in the spectral mapping mode. We reduced this IRS mapping observation using the standard pipeline (version C18.18). First, we subtracted the background emission and removed rogue pixels using IRSCLEAN. Then, we projected the single IRS pointings into a grid similar to CUBISM (Smith et al. 2007). From the data cube, we extracted the spectra using a 7.7 arcsec × 7.7 arcsec and a 17.8 arcsec × 17.8 arcsec square aperture centred at the nuclei in the short-low (SL; 7.6–14 μm) and long-low (LL; 14–36 μm) cubes, respectively. A point-source aperture correction was applied based on the IRS mapping observations of stars. There is a good agreement between the continuum levels at the overlapping spectral ranges of the different modules (SL and LL). This suggests that the mid-IR emission is dominated by a point-like source at the spatial resolution of IRS (∼2–9 arcsec, depending on the wavelength). The IRS spectrum is shown in Fig. 2 along with the MIPS and IRAC photometry.

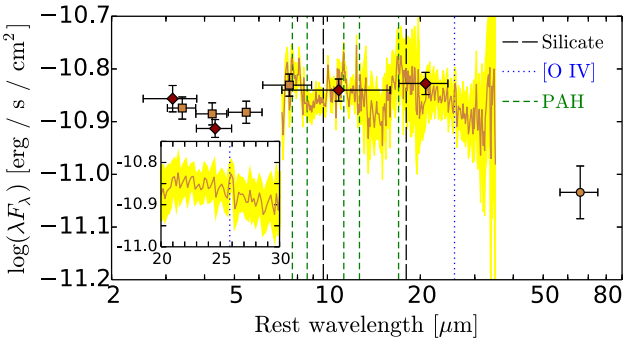

Figure 2. *Spitzer* spectroscopy and photometry of 1H 0323+342 taken in 2008 September. The IRS spectrum is shown in ochre with its error region in yellow. Simultaneous photometry from IRAC and MIPS are shown with squares and a circle, respectively. For comparison, later *WISE* photometry points are shown with red diamonds. The wavelengths of the broad 9.7 and 18 μm silicate features are marked with black long dashed lines; the wavelengths of PAH features are marked with green short dashed lines and that of the [O IV] λ25.8 μm forbidden emission line is marked with a blue dotted line (this is also shown in the inset plot).

We measured the possible [O IV] λ25.89 μm emission line in the IRS spectrum. To do so, we fit the 20–32 μm region with a Gaussian profile and the underlying continuum as a power-law of the form $F_\lambda = a(\lambda/b)^{-c}$, where the constants a, b, and c are free parameters in the fit. We find the Gaussian line has a central, rest-frame wavelength of $25.92^{+0.03}_{-0.04}$ μm, consistent with the [O IV] line. From the fitted Gaussian, which has an FWHM $= 0.26 \pm 0.04$μm, we calculate an integrated luminosity in the line $\log(L_{[\mathrm{O\,IV}]}) = 41.3\,\mathrm{erg\,s^{-1}}$.

1H 0323+342 was detected at 70 μm using MIPS. The data reduction was performed using the MOPEX analysis tool. Following the prescription in the MIPS instrument handbook v3.0, source counts were extracted from a circular region of radius 35 arcsec and the background counts were taken from an annulus with inner and outer radii of 39 and 65 arcsec, respectively. The photometric uncertainty was calculated using equation (1) in Carpenter et al. (2008). The source was found to have a flux density 207 ± 2 mJy, equivalent to a flux of $(8.69 \pm 0.08) \times 10^{-12}\,\mathrm{erg\,s^{-1}\,cm^{-2}}$.

2.2.2 WISE

The *Wide-field Infrared Survey Explorer* (*WISE*; Wright et al. 2010) telescope was launched in 2009 December with the aim of conducting an all-sky survey in the IR. It observes in four photometric bands simultaneously: W1 (3.4 μm), W2 (4.6 μm), W3 (12 μm), and W4 (22 μm). Photometry for the source 1H 0323+342 was obtained in each of these bands from the AllWISE Source Catalog[2]. The photometric magnitudes were calculated from multiple observations (24 for W1 and W2, 12 for W3 and W4) recorded during the survey. The observation start and end dates correspond to those listed in the online long form catalogue.

[2] http://irsa.ipac.caltech.edu/

2.2.3 2MASS

1H 0323+342 was observed as part of the Two Micron All-Sky Survey (2MASS), which was conducted between 1997 and 2001. We obtained measurements in the J, H, and K_S bands from the 2MASS All-Sky Point Source Catalog[3] (Skrutskie et al. 2006). The S/N in these bands were 99.9, 95.3, and 131.0, respectively.

2.2.4 GALEX

The *Galaxy Evolution Explorer* (*GALEX*; Martin et al. 2005) was a dedicated UV space telescope which was launched in 2003 April and operated for 10 years. 1H 0323+342 was detected in the near-UV by *GALEX* during a 96 s exposure on 2011 December 27. Data were extracted from the sixth *GALEX* data release, GR6[4]. The flux was dereddened using the same procedure as for the *XMM–Newton* OM fluxes.

2.3 Data sampling the jet emission

At both the very low and very high frequency ends of the SED, we have data which sample the emission from the relativistic jet.

2.3.1 Effelsberg and IRAM

Radio light curves and SEDs of 1H 0323+342 were produced as part of the *Fermi*-GST Multiwavelength Monitoring Alliance (F-GAMMA; Fuhrmann et al. 2016b) monitoring programme. The observations were conducted between 2010 July 31 and 2014 March 11. Flux densites at 2.64, 4.85, 8.35, 10.45, 14.60, 23.05, 32.00, and 43.05 GHz were obtained at the 100 m Effelsberg telescope. 86.24 and 142.33 GHz readings were made at the 30 m IRAM telescope. For our SED, we have taken the mean flux densities and their standard deviations as reported in table 8 of Angelakis et al. (2015)[5]; we refer the reader to this paper for further details.

2.3.2 Planck

We complemented the low-frequency data with non-simultaneous *Planck* observations taken from the latest version of the *Planck* Catalog of Compact Sources[6] (PCCS2; Planck Collaboration XXVI 2016) that compiles all sources, both Galactic and extra-galactic, detected with high confidence over the full sky during the period between 2009 August and 2013 August. This catalogue contains average intensity information for the sources which may have been observed more than once.

Using a cone search of 1 arcmin, clear association with 1H 0323+342 was found at 100 and 143 GHz in the good-quality PCCS2 catalogues, and in addition at 217 GHz, taken from the PCCS2E catalogue. The catalogue gives multiple flux density estimates, the source associated with 1H 0323+342 being clearly identified on the cutout images; the photometry reported in Table 1 is from Gaussian fitting method.

[3] Also available from the Infrared Science Archive, see note 2.
[4] http://galex.stsci.edu/GR6/
[5] In this paper our source is named J0324+3410.
[6] http://irsa.ipac.caltech.edu/data/Planck/release2/catalogs/

2.3.3 Fermi

The Large Area Telescope (LAT; Atwood et al. 2009) on board the *Fermi* satellite detects γ-ray photons with energies between 20 MeV and above 300 GeV. The source 1H 0323+342 is listed in the second catalogue of flaring γ-ray sources detected with the Fermi All-sky Variability Analysis[7] (FAVA), a tool that blindly searches for transients over the entire sky observed by the LAT (Abdollahi et al. 2017). We analysed a subset of those data over the period 2015 August 1 to 2015 September 30, covering the date of the *XMM–Newton* observation, using the publicly available Science Tools v10r0p53. It appears that the source was in a low state.

Photons in a circular region of interest (RoI) of radius 10°, centred on the position of 1H 0323+342, were considered. The PASS 8 instrument response functions (event class 128 and event type 3) corresponding to the P8R2_SOURCE_V6 response were used together with a zenith-angle cut of 90°. The Galactic diffuse emission has been modelled using the file gll_iem_v06.fits (Acero et al. 2016) and the isotropic background using iso_P8R2_SOURCE_V6_v06.txt. Assuming a power-law spectral shape for 1H 0323+342, a binned likelihood analysis yields a detection with a Test Statistic TS = 11.26 ($\approx 3.4\sigma$) with a flux of $F_{0.1-100\mathrm{GeV}} = (4.65 \pm 1.68) \times 10^{-8}\,\mathrm{cm}^{-2}\,\mathrm{s}^{-1}$ and a photon index of $\Gamma = 2.98 \pm 0.33$.

To do this, the fit was performed iteratively, with all the sources from the 3FGL catalogue within 14° around 1H 0323+342 included, with fixed parameters for those more than 10° away to account for event leakage in the RoI due to the large PSF at low energies. In a second step, the sources contributing to less than a TS of 9 and to less than 5 per cent of the total number of counts in the RoI have their parameters frozen. The only free parameters in the end are those of sources less than 3° away from 1H 0323+342, if not frozen in the previous step and the normalizations of the Galactic and isotropic diffuse emissions.

2.4 Supplementary X-ray data

We present *Swift* X-ray telescope (XRT) monitoring data covering the same frequency and time period as the *XMM–Newton* observation. Finally, hard X-ray spectra from both *NuSTAR* and *Swift* burst alert telescope (BAT) bridge the frequency range between the *XMM–Newton* X-ray spectra and the γ-ray emission recorded by *Fermi*.

2.4.1 Swift XRT

Swift monitoring of the source was conducted from 2015 August 2 to December 24, with snapshot observations of approximately 2 ks durations taken with an average ≈6 day cadence. We reduced the data from the 12 observations taken between 2015 August 2 and September 29, around the time of the 81 ks *XMM–Newton* observation (see Section 2.1.3) and covering the period of the *Fermi* observations we use in this paper (see Section 2.3.3). The XRT products were created using XRTPIPELINE v0.13.2. The source extraction regions were a 47-arcsec-radius circle centred on the source (corresponding to the 90 per cent encircled energy radius at 1.5 keV) and the background regions were 141 arcesc circular regions offset from the source, in an area free of field sources. The spectra were extracted using XSELECT and ancilliary response files were created with XRTMKARF. The observations of August 11 and September

[7] https://fermi.gsfc.nasa.gov/ssc/data/access/lat/FAVA/

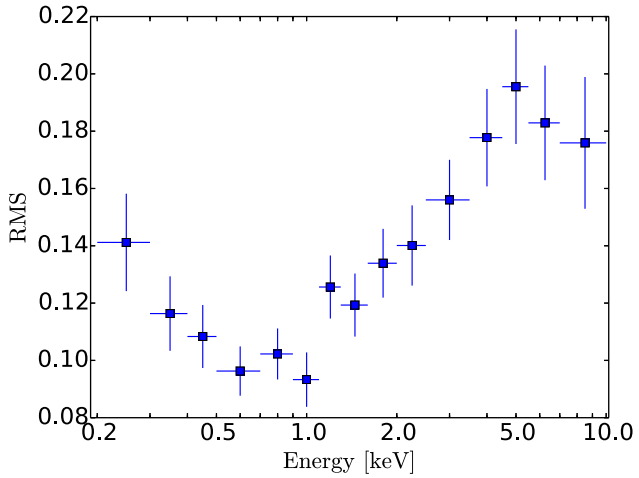

Figure 3. The X-ray RMS fractional variability spectrum of 1H 0323+342. Fifteen light curves spanning the 0.2–10.0 keV energy range were created from the *XMM–Newton* EPIC pn event file with time bins of 500 s.

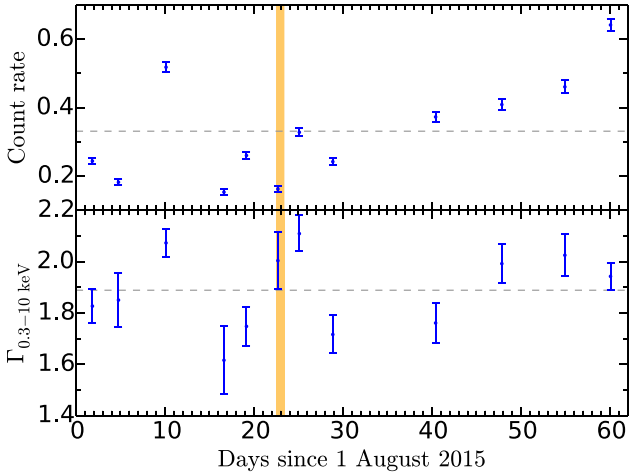

Figure 4. Upper panel: *Swift* XRT 0.3–10.0 keV count rates in counts s^{-1}. Lower panel: The X-ray photon index Γ of the best-fitting absorbed power-law model fit to the *Swift* spectrum. The mean values of both count rate and Γ are shown as grey dashed lines. The time span of the *XMM–Newton* observation is highlighted in orange.

29–30 (OBS IDs 00036533056 and 00036533066) both had count rates slightly exceeding 0.5 counts s^{-1} and were investigated for pile-up. The wings of the PSF beyond 15 arcsec from the centre were fitted with a King function with the parameters $r_c = 5.8$ and $\beta = 1.55$ fixed (see Moretti et al. 2005 for further details). This function was then extrapolated into the inner regions. The deviation of the data from the model King function in the centre of the PSF was very marginal, so for our purposes it was unnecessary to extract the spectra from an annular region. Using GRPPHA, we rebinned each spectrum to contain a minimum of 20 counts per bin such that they were suitable for a χ^2 analysis.

2.4.2 NuSTAR

A 200 ks exposure of the source was taken using *NuSTAR* in 2014 March. The data reduction is detailed in Landt et al. (2017). Here we use the co-added, time-averaged spectra from both focal plane modules FPMA and FPMB.

2.4.3 Swift BAT

We include catalogue data from the *Swift* BAT 70-month all-sky survey. The survey includes all sources detected in the hard X-ray energy range 14–195 keV in the period 2004 December and 2010 September (Baumgartner et al. 2013). The 14–195 keV photon index and flux were reported to be $\Gamma = 1.73$ and 2.993×10^{-11} erg s^{-1} cm^{-2}, respectively.

3 X-RAY ANALYSIS

3.1 Variability

3.1.1 Short-term variability

We produced an RMS spectrum by creating light curves with 500 s time bins in 15 energy bands between 0.2 and 10.0 keV. The excess RMS variability and its error were calculated for each light curve using the HEASARC FTOOL LCSTATS; these are plotted in Fig. 3. The spectrum clearly shows a break around 1 keV with the soft and hard spectral components exhibiting different variability behaviour.

3.1.2 Medium-term variability

Each of the 12 *Swift* spectra taken between 2015 August 2 and September 30 was fitted with a simple absorbed power-law model in XSPEC. To construct the light curve shown in Fig. 4, we report the 0.3–10.0 keV count rates and also the best-fitting X-ray photon indices. The count rates vary by a factor of 4 over this 2-month period and the *XMM–Newton* observation was taken during a period of particularly low activity. The photon indices are poorly determined because of the limited S/N spectra, but by comparing the count rates and photon indices it can be seen that the source does not follow a simple 'softer-when-brighter' pattern of behaviour.

3.1.3 Longer-term variability

The *Swift* count rates in our main time interval of interest are ≈0.3 counts s^{-1}, which are around the lowest values recorded in the five-and-a-half year light curve shown in Paliya et al. (2014) (their fig. 1). As noted in Landt et al. (2017), we observed only an ∼30 per cent variation in 2–10 keV flux between the three epochs of *Swift* data (2013 August, 2014 December, and 2015 September) taken around the same time as our IR and optical spectra. In the corresponding *Swift* UVOT data, some variability in the *B*, *U*, *UVW*1, and *UVW*2 filters was observed, but only ∼20–30 per cent at the 2σ–3σ level.

3.2 X-ray spectral analysis

The X-ray spectral fitting of the *XMM–Newton* data was performed in XSPEC v12.9.0n (Arnaud 1996). In all models we included a Galactic absorbing column (PHABS), initially adopting the D&L90 value $N_H^{Gal} = 1.46 \times 10^{21}$ cm^{-2}. Cross-normalization factors were included to account for differences in calibration between the three EPIC detectors; these did not vary by more than 5 per cent.

3.2.1 The shape of the X-ray spectra

A single power-law (with $\Gamma_{2-10\ \mathrm{keV}} \approx 1.7$) fit to the 2–10 keV data shows an excess of soft emission below ≈2 keV (see Fig. 5(a)).

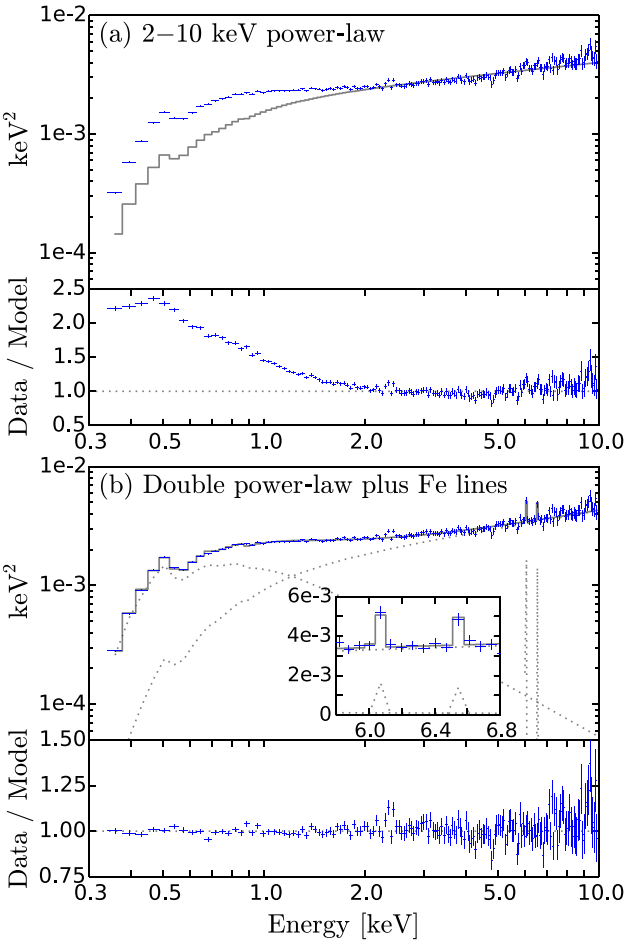

Figure 5. Fits to the *XMM–Newton* EPIC-pn X-ray spectrum of 1H 0323+342 taken during the 2015 August 23–24 observation. Fits were performed to all three spectra (pn, MOS1, and MOS2) simultaneously; for clarity we show only the pn data here. Upper panels show the data (crosses) with the total model (histograms) and the individual model components (dotted lines) for each of the three detectors in units of photons $cm^{-2}\,s^{-1}\,keV^{-1}$; lower panels show the data/model ratios. The model shown in (a) includes fixed $N_H^{Gal} = 1.46 \times 10^{21}\,cm^{-2}$; the model shown in (b) has free $N_H^{Gal} = 2.33 \times 10^{21}\,cm^{-2}$.

Consequently, a single power-law (with $\Gamma \approx 2.1$) to the whole 0.3–10 keV range results in a very poor fit to the data with a reduced chi-square $\chi^2_\nu = 9.69$. These fits, and the shape of the RMS spectrum shown in Fig. 3, clearly indicate that a continuum model with at least two components is required to fit the data.

A double power-law model (the first model in Table 3) is not a very good fit to the data. In the course of our modelling, we noticed that our models overpredict the data at energies below ≈0.5 keV. Additionally, the deabsorbed spectra do not rise towards lower energies to connect smoothly to the contemporaneous optical/UV photometry. These issues could be resolved by including some additional absorption in our models. Allowing N_H^{Gal} to be a free parameter, we consistently find it rises to a value $\approx 2.2 \times 10^{21}\,cm^{-2}$, approximately 50 per cent greater than the D&L90 value, and then gives a statistically significant improvement in the fits. We note that these values are similar to the total (H I plus H_2) Galactic column of $2.17 \times 10^{21}\,cm^{-2}$ found by Willingale et al. (2013). A double power-law model with free N_H^{Gal} is a significant improvement with $\Delta\chi^2 = 162$ and an *F*-test probability > 99.99 per cent. The implications of deabsorbing the EPIC X-ray spectrum with this higher N_H^{Gal} are discussed further in Section 5. The fit can be further improved by the inclusion of two narrow emission lines, as is described in the next section.

Table 3. Results of X-ray spectral fits.

Model	Parameter	Value
PHABS ×	N_H^{Gal} (cm^{-2})	$(1.46) \times 10^{21}$ [a]
(POWERLAW +	Γ_1	2.54 ± 0.02
	norm.	$\left(2.47^{+0.04}_{-0.05}\right) \times 10^{-3}$
POWERLAW)	Γ_2	1.06 ± 0.04
	norm.	$(4.7 \pm 0.4) \times 10^{-4}$
	χ^2/d.o.f.	$731/496 = 1.47$
PHABS ×	N_H^{Gal} (cm^{-2})	$(2.31 \pm 0.08) \times 10^{21}$
(POWERLAW +	Γ_1	3.54 ± 0.09
	norm.	$(2.10 \pm 0.04) \times 10^{-3}$
POWERLAW)	Γ_2	$1.49^{+0.02}_{-0.03}$
	norm.	$(1.34 \pm 0.06) \times 10^{-3}$
	χ^2/d.o.f.	$569/495 = 1.15$
PHABS ×	N_H^{Gal} (cm^{-2})	$(2.33 \pm 0.08) \times 10^{21}$
(POWERLAW +	Γ_1	3.59 ± 0.09
	norm.	$(2.06 \pm 0.04) \times 10^{-3}$
POWERLAW +	Γ_2	1.52 ± 0.02
	norm.	$\left(1.39^{+0.06}_{-0.07}\right) \times 10^{-3}$
ZGAUSS +	E (keV)	$6.43^{+0.03}_{-0.02}$
	norm.	$(3.4 \pm 0.8) \times 10^{-6}$
	EW (eV)	34 ± 8
ZGAUSS)	E (keV)	6.95 ± 0.04
	norm.	$(2.4 \pm 0.8) \times 10^{-6}$
	EW (eV)	28 ± 9
	χ^2/d.o.f.	$540/491 = 1.10$

Note. [a]Parameter was frozen during the fitting procedure. Errors are quoted at the 1σ level. The best-fitting model is plotted in Fig. 5.

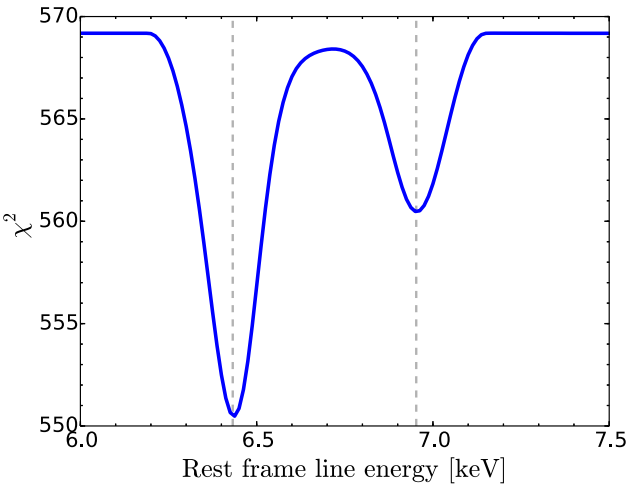

Figure 6. Variation in the χ^2 fit statistic with the rest frame line energy of a narrow (fixed width $\sigma = 10$ eV) Gaussian emission line. Best-fitting line energies of 6.43 and 6.95 keV are indicated with dashed lines.

3.2.2 *Iron line emission features in the X-ray spectra*

Fig. 6 shows that the fit statistic can be further improved by the addition of narrow emission lines at ≈6.4 and ≈6.9 keV. We first added a broad line at ≈6.4 keV, but the fitting procedure reduced the width of the line to below the detector resolution, which is

unphysical, and so instead we fit a narrow line of fixed width $\sigma = 10$ eV. We find that its rest-frame energy is $6.43^{+0.03}_{-0.02}$ keV, consistent with neutral Fe Kα emission, and inconsistent with the 6.7 keV energy of Fe XXV. The fit is improved by a $\Delta\chi^2 = 19$ for three additional free parameters to $\chi^2_\nu = 550/493 = 1.12$, giving an F-test probability of 99.97 per cent compared to the model with no emission line. The line flux is $\left(3.1^{+0.7}_{-0.4}\right) \times 10^{-14}$ erg s^{-1} cm^{-2} and its equivalent width (EW) is low at 34 ± 8 eV, which we discuss in Section 5.

The fit is improved by a further $\Delta\chi^2 = 10$ with the inclusion of a second narrow Gaussian at 6.95 ± 0.04 keV, consistent with Fe XXVI. Clearly this is a weaker line than the neutral Fe Kα and we estimate its EW to be 28 ± 9 eV. Our final X-ray spectral fit has a $\chi^2_\nu = 1.10$, its parameters are given in Table 3, and it is shown in Fig. 5(b).

4 THE ORIGIN OF THE γ-RAY EMISSION

The γ-ray emission from high accretion-rate blazars such as FSRQs and γ-NLS1s is thought to be produced by the external Compton (EC) mechanism whereby an ambient field of soft seed photons external to the jet is Compton upscattered by relativistic leptons within the jet. Emission from the accretion disc and its X-ray corona, the BLR, and dusty torus can all potentially contribute to this external seed photon field. Our new approach here is to determine the external photon field from our quasi-simultaneous IR-to-X-ray data which also samples the accretion flow. Our parametrization of the external photon field is presented below in Section 4.1. In Section 4.2, we then use a jet emission code to upscatter the external photon field and fit this to the full multiwavelength SED, determining the site of the γ-ray emission, and the dominant source of seed photons.

4.1 Determining the external photon field

It is common in modelling EC emission to assume a standard external seed photon field which is upscattered by particles in the relativistic jet. Instead, we determine the external photon field of this particular source from our data; the results are presented in Table 4. In Table 5 we summarize our findings and compare these to the standard assumptions made in the modelling of the photon field by Ghisellini & Tavecchio (2009, hereafter G&T09), on which our jet emission code is based.

4.1.1 The accretion flow emission

The accretion flow emission is dominated by radiation from a disc of material accreting on to the BH. This emission results from the radiative release of gravitational potential energy via viscous forces in the disc. The radiative efficiency η of the accretion disc is determined by the location of its innermost stable circular orbit $R_{\rm isco}$, inside of which material plunges into the BH. For a given BH mass and emissivity profile, discs with a smaller $R_{\rm isco}$ have a greater radiating surface area and hence a greater η. The location of $R_{\rm isco}$ is set by the spin[8] of the BH; a maximally spinning BH has $R_{\rm isco} = 1R_{\rm g} = GM_{\rm BH}/c^2$ a non-rotating BH has $R_{\rm isco} = 6R_{\rm g}$.

For low-mass and high accretion-rate BHs, the Wien tail of the accretion disc emission can extend into the soft X-ray bandpass. However, the accretion discs of supermassive BHs are not generally expected to emit much X-radiation. Most of the observed X-ray emission results from the Compton upscattering of photons by populations of hot electrons near to the BH. One such region is the optically thin corona of the accretion disc, which produces X-ray emission well-represented as a power-law extending up to ≈150 keV. As well as this power-law, many AGNs also show evidence of a second Comptonization region which is cooler and optically thicker than the corona. The emission from this region is observed as an excess of soft X-ray emission above the coronal power-law, so it is often dubbed the 'soft excess'. When modelled as a thermal component, the soft excess has a remarkably constant temperature (0.1–0.2 keV) across sources covering a wide range of BH masses and Eddington ratios (e.g. Gierliński & Done 2004; Porquet et al. 2004).

The continuum emission from the accretion flow of many AGNs can therefore be represented by three components: the accretion disc emitting mostly in the optical/UV, plus a two Comptonization regions producing soft excess and coronal X-rays. An energy-conserving version of this simple concept (OPTXAGNF, included in the current version of XSPEC) is described by Done et al. (2012). It includes a number of modifications to the simpler Shakura & Sunyaev (1973) accretion disc spectrum which are relevant to the modelling of the accretion flows of NLS1s. First, for low-mass, high accretion rate systems such as NLS1s the inner disc is very hot and is not fully thermalized at all radii. The code applies an appropriate colour-temperature correction to the accretion disc spectrum. Secondly, the standard disc does not extend all the way down to $R_{\rm isco}$; instead, it truncates at the coronal radius $R_{\rm cor}$. Inside of $R_{\rm cor}$ a fraction $f_{\rm pl}$ of the power emerges as the coronal power-law emission. The remaining fraction $(1 - f_{\rm pl})$ of the power produces the soft excess. Here we use the XSPEC local model OPTXCONV (Done et al. 2013), an extension of OPTXAGNF that approximates relativistic corrections to the spectrum, which are particularly pronounced at low inclinations and high spins.

At wavelengths longer than 1 μm, the Wien tail of blackbody emission from hot dust in the torus is dominant over the accretion disc emission. The 1 μm region is covered by both our GNIRS (near-IR) and Keck (optical) spectra; we extracted from these spectra data points sampling the emission line free continuum so that we can also parametrize the hot dust emission.

We include our *NuSTAR* spectrum, taken 17 months prior to the *XMM–Newton* observation, thereby extending our SED up to 79 keV. We note that although similar in levels of flux, the photon index of our *NuSTAR* spectrum ($\Gamma = 1.80 \pm 0.01$) is softer than the index we determine in the overlapping energy range of *XMM–Newton* spectrum ($\Gamma_{3-10\,\rm keV} = 1.59 \pm 0.02$). It is known that a calibration issue with *XMM–Newton* results in harder spectral indices above ≈3 keV than those determined from other X-ray telescopes. For example, Ingram et al. (2017) found that the spectral index of their *XMM–Newton* spectrum was $\Delta\Gamma = 0.22$ lower than that of their *NuSTAR* spectrum taken simultaneously, very similar to the discrepancy we see here. In our non-simultaneous data the difference in spectral shape could be due to this miscalibration, but may, of course, result from a genuine spectral evolution between the two observations.

The mass accretion rate $\dot{M}$ through the outer accretion disc is constrained by the observed optical continuum emission. We set the outer accretion disc radius to be equal to the self-gravity radius $R_{\rm sg}$, beyond which the disc fragments. The X-rays are emitted from a region between $R_{\rm cor}$ (a model parameter which we fit) and $R_{\rm isco}$, the latter being determined by $a_\star$. Since we have no prior input on $a_\star$ (from e.g. broad Fe Kα), we test both zero- and high-spin cases with $a_\star$ fixed to 0.0 or 0.8. As well as fitting a model in which all

[8] Here we use the dimensionless spin parameter $a_\star = Jc/GM^2_{\rm BH}$, where J is the angular momentum of the BH.

Table 4. Results from spectral fits to the deabsorbed IR to hard X-ray SED.

	$a_\star$	$L/L_{\rm Edd}$	$\dot{M}$ ($M_\odot$ yr^{-1})	$R_{\rm cor}$ ($R_{\rm g}$)	$R_{\rm out}$ ($R_{\rm g}$)	log ($L_{\rm AD}$) (erg s^{-1})	$kT_{\rm e}$ (keV)	τ	$f_{\rm pl}$	$\Gamma_{\rm cor}$	log ($L_{\rm cor}$) (erg s^{-1})	$T_{\rm tor}$ (K)	log ($L_{\rm tor}$) (erg s^{-1})	$R_{\rm tor}$ (ld)	χ^2/dof
	(1)	(2)	(3)	(4)	(5)	(6)	(7)	(8)	(9)	(10)	(11)	(12)	(13)	(14)	(15)
(a)	0.0[a]	0.60	0.44	27.2	2450	45.27	0.30	11	0.3[a]	1.76	44.53	1720	44.10	292	799/236
(b)	0.0[a]	0.60	0.44	24.3	2440	45.30	0.22	12	0.3[a]	2.70	44.54	1730	44.10	297	687/232
(c)	0.8[a]	0.81	0.30	13.5	3380	45.55	0.03	100[b]	0.3[a]	3.25	44.83	1610	44.10	485	916/232

Note. The columns are: (1) dimensionless BH spin; (2) Eddington ratio; (3) mass accretion rate; (4) outer coronal radius in gravitational radii, $R_{\rm g} = 2.95 \times 10^{10}$ m $=1.14 \times 10^{-3}$ light days; (5) outer accretion disc radius which was set to $R_{\rm sg}$; (6) luminosity of the accretion disc; (7) electron temperature of the soft Comptonization region; (8) optical depth of the soft Comptonization region; (9) fraction of the disc power below $R_{\rm cor}$ emitted in the power-law tail; (10) photon index of the power-law tail; (11) luminosity of the power-law tail; (12) temperature of the dusty torus; (13) luminosity of the IR radiation from the torus; (14) the dusty torus inner radius in light days, see Section 4.1.3 in the text for details; (15) the χ^2 statistic over the number of degrees of freedom (d.o.f.) in the model. [a]Parameter was frozen during the fitting procedure. [b]Parameter has reached the limit of the allowed range. $\dot{M}$ and $R_{\rm tor}$ are not model parameters but have been derived from our results. These models are plotted in Fig. 7.

Table 5. Differences between the external photon field parameters we determined and those calculated from standard assumptions.

Parameter		Units	Standard scaling	Standard value	Our value
Eddington ratio	$L/L_{\rm Edd}$		Davis & Laor (2011) equation (7)[a]	0.66	0.60
Outer corona radius	$R_{\rm cor}$	$R_{\rm g}$		60	24
Outer disc radius	$R_{\rm out}$	$R_{\rm g}$		1000	2440
Disc luminosity	log ($L_{\rm AD}$)	erg s^{-1}		45.26	45.30
Corona luminosity	log ($L_{\rm cor}$)	erg s^{-1}	$= 0.1L_{\rm AD}$	44.26	44.54
BLR luminosity	log ($L_{\rm BLR}$)	erg s^{-1}	$= 0.1L_{\rm AD}$	44.26	43.33
BLR radius	$R_{\rm BLR}$	$R_{\rm g}$ (ld)	$= 5.29R_0 \left(\frac{L_{\rm AD}}{10^{45}{\rm erg\ s^{-1}}}\right)^{1/2}$	4.58×10^4 (52)	2.72×10^4 (30)
Dusty torus luminosity	log ($L_{\rm tor}$)	erg s^{-1}	$= 0.3L_{\rm AD}$	44.74	44.10
Dusty torus radius	$R_{\rm tor}$	$R_{\rm g}$ (ld)	$= 132R_0 \left(\frac{L_{\rm AD}}{10^{45}{\rm erg\ s^{-1}}}\right)^{1/2}$	1.20×10^6 (1400)	2.63×10^5 (300)
Dust temperature	$T_{\rm tor}$	K		370	1730

Notes. The scaling parameter $R_0 = 1.89 \times 10^{16}$ cm. See Gardner & Done (2018) for further details. [a]Here we make another measure of the Eddington ratio, scaled from the optical luminosity determined by Landt et al. (2017) and assuming a radiative efficiency $\eta = 6$ per cent in the calculation of the bolometric luminosity $L = \eta \dot{M} c^2$.

of the hard X-ray emission originates from the corona, we also fit models which include a hard X-ray contribution from the jet. We model the jet as a broken power-law to allow for some curvature in its shape over the broad energy range. In all models we fix $f_{\rm pl}$ to 0.3 (Done et al. 2012; Jin et al. 2012). From our models we are able to determine several parameters which we will use to set the external photon field; namely: the size scales and luminosities of the accretion disc, its corona, and the hot torus dust, as well as the temperature of the dust (see Section 4.1.3).

The results are presented in Table 4 and plotted in Fig. 7. Both zero spin models represent the data reasonably well, and the accretion disc and hot dust parameters are very similar. The soft excess temperature $kT_{\rm e} = 0.30$ keV of the zero spin, no jet model is slightly higher than is typically observed ($\langle kT_{\rm e} \rangle = 0.12 \pm 0.02$ keV; Gierliński & Done 2004). The zero spin plus jet model shows that if the harder X-rays originate from the relativistic jet then it is possible to describe the rest of the optical-to-X-ray SED with a very typical NLS1 model.

All three models imply a relatively high Eddington ratio $L/L_{\rm Edd} \approx 0.6$–$0.8$ but not super-Eddington accretion. We estimate the accretion disc luminosity at $L_{\rm AD} = 2.1 \times 10^{45}$ erg s^{-1} for the zero BH spin cases or ≈80 per cent greater in the high-spin case. However, the high spin model is a poorer fit to the data and cannot accommodate a soft excess component in the *XMM–Newton* bandpass. The fitting procedure lowers $kT_{\rm e}$ and raises τ to its maximum permitted value to force the soft excess emission out of the *XMM–Newton* bandpass so as to minimize the soft X-ray power. The soft excess thus appears to have a lower temperature than the inner accretion disc, which is unphysical in this model since the soft Comptonization region is at smaller radii than the disc, implying that it should be hotter. If we remove this (unseen) soft excess component by setting $f_{\rm pl} = 1$, then we must lower $R_{\rm cor}$ to reduce the power in the coronal component. Consequently, the inner radius of the accretion disc is lower and the accretion disc emission appears in the soft part of the X-ray spectrum, overpredicting the data. In summary, an energy-conserving, high-spin model produces more soft X-ray power than is seen in the data.

With the available data, we are unable to rule out the case that the corona produces all of the 2–10 keV X-ray emission. However, we prefer the zero spin model that includes a contribution from the jet for the following reasons. First, it gives a statistically significant improvement in the fit compared to the no-jet model with $\Delta\chi^2 = 112$ for four additional free parameters. Secondly, if we allow for jet emission at the hard energies, we recover parameters which are typical for a NLS1, showing a soft excess of temperature $kT_{\rm e} = 0.22$ keV and a soft-spectrum X-ray corona. Thirdly, the similarity of the hard X-ray photon indices (*XMM–Newton*: $\Gamma_{3-10\,{\rm keV}} = 1.59 \pm 0.02$, *NuSTAR*: $\Gamma_{3-79\,{\rm keV}} = 1.80 \pm 0.01$, and *Swift* BAT: $\Gamma_{14-195\,{\rm keV}} = 1.73 \pm 0.02$) are suggestive of a single spectral component, given that the discrepancy between *XMM–Newton* and *NuSTAR* spectral shapes may be the result of a cross-calibration problem, as noted in Section 4.1.1. Taken together with the *Fermi* data, the hard X-rays appear to be the low-energy side of the Compton hump, as we will subsequently show in our jet models. In the following sections we proceed with the parameters determined from the model with zero BH spin plus a jet.

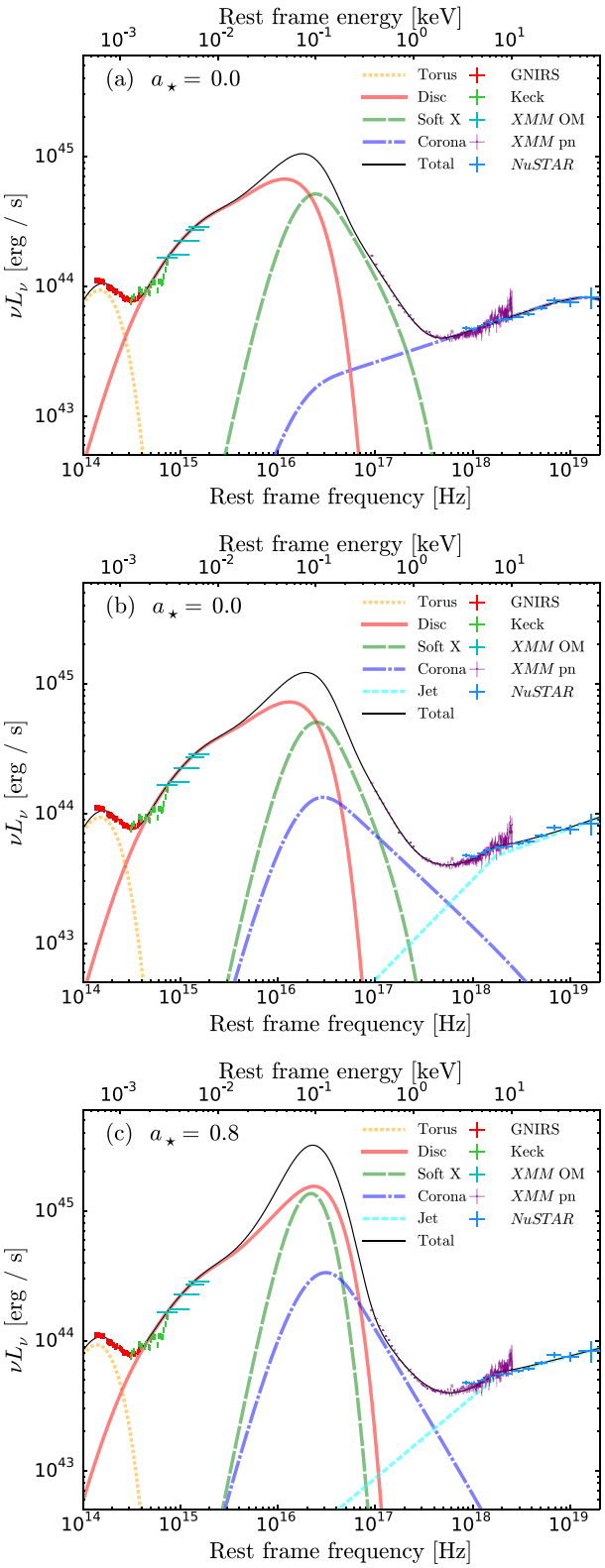

Figure 7. IR to hard X-ray SEDs of 1H 0323+342. The data are modelled by the energy-conserving accretion model OPTXCONV which calculates the emission from the accretion disc, corona, and soft Comptonization region ('Soft X'). In addition, we have added a blackbody modelling hot dust emission in the IR and, in models (b) and (c), a broken power-law to model hard X-ray emission from the jet. See Table 4 in the text for the model parameters.

4.1.2 *The BLR luminosity and radius*

The emission from the BLR is another important component of the external photon field which can be Compton-scattered to higher energies by the particles in the relativistic jet. This emission region is located beyond the accretion disc, on a typical scale of several light-weeks. The two relevant measures for our jet modelling are then the luminosity and radius of the BLR. We have estimated the BLR luminosity following Celotti, Padovani & Ghisellini (1997) as:

$$L_{\rm BLR} = \Sigma_i L_{i,\rm obs} \frac{\langle L^*_{\rm BLR} \rangle}{\Sigma_i L^*_{i,\rm est}}, \quad (1)$$

where $\Sigma_i L_{i,\rm obs}$ is the sum of the measured luminosities of the observed broad lines, scaled by the ratio of the estimated total BLR luminosity $L^*_{i,\rm est}$ to the estimated luminosities of the observed broad lines. Both estimates were taken from the results of Francis et al. (1991) and, in the case of Hα, from Gaskell, Shields & Wampler (1981). The BLR luminosity is determined most accurately based on the actual measurement of the strongest emission lines, e.g. Lyα, C IV, Hα, etc. Our optical spectrum covers two of the relevant broad emission lines, namely Hβ and Hα. For their broad components we get a luminosity of $\log L_{\rm H\beta} = 42.02\,{\rm erg\,s^{-1}}$ and $\log L_{\rm H\alpha} = 42.44\,{\rm erg\,s^{-1}}$, respectively (Landt et al. 2017), which results in a total BLR luminosity of $\log L_{\rm BLR} = 43.33\,{\rm erg\,s^{-1}}$.

We have estimated the BLR radius in two ways, using both the near-IR and optical radius–luminosity relationships. The near-IR radius–luminosity relationship presented by Landt et al. (2011, 2013) is based on the rest-frame 1 μm continuum luminosity, which, as these authors show, is still dominated by the ionizing accretion disc luminosity. Landt et al. (2017) measured this quantity in the near-IR spectrum to be $\log \nu L_{1\,\mu\rm m} = 43.92\,{\rm erg\,s^{-1}}$. The derived BLR radius is then 23 light-days. The optical radius-luminosity relationship was most recently calibrated by Bentz et al. (2013) using the rest-frame 5100 Å continuum luminosity. From their optical spectrum, Landt et al. (2017) measured this quantity to be $\log \nu L_{5100\text{Å}} = 44.05\,{\rm erg\,s^{-1}}$; the derived BLR radius is then 39 light-days. The two values resulting from the near-IR and optical radius-luminosity relationships are similar within the errors, which, when taken from the scatter in the relations, are ∼40–50 per cent. In the following jet modelling, we have used the average between the two values of 31 light-days.

We note that Wang et al. (2016) calculated a BLR radius of $14.6^{+7.8}_{-2.9}$ light-days from the measurement of the lag in the response of Hβ to changes in the continuum flux. Whilst their estimate of the BLR radius is smaller than our two values, it has a large positive error and is discrepant with our average value by only $\approx 2\sigma$.

4.1.3 *The dusty torus luminosity and radius*

The dusty torus is the most extended AGN component which contributes to the external photon field that is upscattered by the jet. This region is located farther away from the BH than the BLR; indeed its hottest, innermost part may be the outermost boundary of the BLR, on scales of light-months. The relevant measures for our jet modelling are the luminosity, radius, and temperature of the hot dust in the torus. The luminosity and temperature of the hot dust result directly from the blackbody fit to the near-IR continuum and are listed in Table 4. We have then estimated the hot dust radius using the theoretical relationship between bolometric luminosity and dust sublimation radius for grains with an average size given by Mor & Netzer (2012). We have assumed that the dust

sublimation temperature corresponds to the hot dust temperature and since we find this value to be $T_{\rm tor} \sim 1700$ K, which is much higher than the sublimation temperature of ∼1400 K for a silicate dust composition, we have used their equation (2) for pure graphite dust[9]. The bolometric luminosity results directly from our accretion disc fits and is listed in Table 4. The resulting hot dust radius is then ≈300 light-days.

4.2 Determining the jet parameters

4.2.1 Calculating the observed jet emission

JET is a single-zone leptonic jet emission code and based on the model presented by G&T09 and coded by Gardner & Done (2018). The jet is modelled as a cone with a half-opening angle ϕ originating at the BH. The jet is viewed by the observer at some angle of inclination i. The model assumes that the jet emission is dominated by radiation from a single spherical 'blob' of radius $R_{\rm diss} = \phi Z_{\rm diss}$, where $Z_{\rm diss}$ is its distance from the BH. The material within the jet moves with a constant bulk Lorentz factor $\Gamma_{\rm BLF}$. Some fraction

$$P_{\rm rel} = \frac{4\pi}{3} R_{\rm diss}^3 m_{\rm e} c^2 \int_{\gamma_{\rm min}}^{\gamma_{\rm max}} \gamma\, Q(\gamma)\, {\rm d}\gamma \qquad (2)$$

of the total jet power $P_{\rm j}$ is used to accelerate electrons within the emission region. The accelerated electrons have Lorentz factors between $\gamma_{\rm min}$ and $\gamma_{\rm max}$ and injected electron population, $Q(\gamma)$, is parametrized as

$$Q(\gamma) = Q_0 \left(\frac{\gamma}{\gamma_{\rm brk}}\right)^{-s_1} \left[1 + \left(\frac{\gamma}{\gamma_{\rm brk}}\right)^{s_2 - s_1}\right]^{-1}, \qquad (3)$$

where s_1 and s_2 are the slopes of the distribution below and above the break Lorentz factor $\gamma_{\rm brk}$, respectively. These electrons then cool by both 'internal' and 'external' mechanisms. The internal processes are the electrons' synchrotron emission (through interaction with the jet's magnetic field) and the Compton upscattering of these synchrotron photons by the electron population which produced them: the sychrotron self-Compton (SSC) process. The 'external Compton' (EC) process cools electrons by the Compton upscattering of photons from the seed photon field external to the jet. The code runs through multiple cooling cycles until the system reaches a steady state. The highest-energy electrons cool fastest and the steady-state distribution is found by calculating the Lorentz factor $\gamma_{\rm cool}$ of electrons that can just cool in the light-crossing time of the emission region and requiring this match the injected distribution below $\gamma_{\rm cool}$.

Finally, the code calculates the observed frame emission which is boosted and blueshifted relative to the jet frame emission due to the bulk motion of the emitting plasma within the jet flow. The observed emission from a region moving with velocity $\beta = v/c$ is a factor δ^3 greater than the intrinsic emission where the Doppler factor $\delta = (\Gamma_{\rm BLF}[1 - \beta \cos i])^{-1}$. The code also outputs the calculated total jet power $P_{\rm j} = P_{\rm rad} + P_{\rm e} + P_B + P_{\rm p}$, which is the sum of the radiative power ($P_{\rm rad}$), the power in the bulk motions of electrons ($P_{\rm e}$), and protons ($P_{\rm p}$) and the Poynting power (P_B).

JET can be used additively with the OPTXCONV code by linking together the parameters $M_{\rm BH}$, $L/L_{\rm Edd}$, i, the comoving distance $D_{\rm c}$ and z. We note that this single-zone model does not calculate all of the radio jet emission. Single-zone models calculate the emission from the base of the jet, but most of the radio emission is produced further out. Synchrotron emission in the modelled zone is strongly self-absorbed below the synchrotron self-absorption frequency, $\nu_{\rm ssa}$, with the spectrum below this falling off in intensity as $I \propto \nu^{5/2}$. The observed radio slope in the SED results from the sum of emission from successive regions further along the jet with lower synchrotron self-absorption frequencies. The JET code does not calculate any emission below $\nu_{\rm ssa}$, but in the plots shown in Fig. 8 we have subsequently added on a ν^0 slope illustrating the emission from multiple zones and we quote $\nu_{\rm ssa}$ in Table 7.

4.2.2 The site of the γ-ray emission

The location of the energy dissipation region $Z_{\rm diss}$ is an important but unknown factor in the determination of the jet SED. It governs the relative importance of the disc, BLR, and torus seed photons in the EC process. Disc photons always arrive from behind the jet and so are de-boosted in the jet frame. However, because the disc is much more luminous than the BLR and torus, disc seed photons may dominate the seed photon energy density seen by the jet if the emission region is very near to the BH. When $Z_{\rm diss} < R_{\rm BLR}$, the BLR photons are boosted in the jet frame, so the BLR component will dominate the EC seed photon energy density further from the disc where $R_{\rm out} < Z_{\rm diss} \lesssim R_{\rm BLR}$. The structure and geometry of the BLR are unknown but it is modelled as a thin spherical shell. Following G&T09, the energy density of BLR seed photons is calculated in three distance ranges: interior to $R_{\rm BLR}$ $U'_{\rm BLR}$ is constant (equation 19 of G&T09); beyond $3R_{\rm BLR}$ it depends on both $Z_{\rm diss}$ and the bulk speed of the jet (equation 20 of G&T09); between $R_{\rm BLR}$ and $3R_{\rm BLR}$ it is calculated as a power-law interpolation. For a $\Gamma_{\rm BLF} = 13$ jet, $U'_{\rm BLR}$ decreases by more than four orders of magnitude between $R_{\rm BLR}$ and $3R_{\rm BLR}$. When $R_{\rm BLR} < Z_{\rm diss} \lesssim R_{\rm tor}$ both the disc and BLR photons are de-boosted in the jet frame and the torus seed photons dominate the energy density.

The issue of whether $Z_{\rm diss}$ is near to, or far from, the BH is contentious and has been much discussed in the literature (see Madejski & Sikora 2016 for a recent overview). The rapid variability of jet emission suggests a compact dissipation region. Under the assumptions of a conical jet that radiates across its entire cross section, this in turn implies a dissipation region relatively near to the central engine. On the other hand, the high energy density of UV photons near to the BH is a source of opacity to γ-rays and suggests a more distant dissipation region, particularly for objects which exhibit very high-energy (TeV) γ-ray emission. Ghisellini & Tavecchio (2015) showed that the dissipation regions of 191 FSRQs were almost always within the BLR radius. Sikora, Begelman & Rees (1994) suggest that it may be Lyα emission from the BLR which provides the dominant source of seed photons encountered by the jet. Conversely, in a study of 36 FSRQ-type blazars, Zheng et al. (2017) found that the dissipation regions were all outside of the BLR, and many were within the region in which the seed photon field is dominated by IR radiation from the torus. Since we have determined the external photon field of 1H 0323+342, we can use this to predict the jet SED for a range of $Z_{\rm diss}$ over three orders of magnitude. We consider the three possibilities that the seed photon field is dominated by the accretion disc ($Z_{\rm diss} = 1280\, R_{\rm g}$: the mean $Z_{\rm diss}$ of FSRQs determined by Ghisellini et al. 2010, hereafter G10); the BLR ($Z_{\rm diss} \approx R_{\rm BLR} = 2.72 \times 10^4 R_{\rm g}$); or the torus ($Z_{\rm diss} \approx R_{\rm tor} = 2.63 \times 10^5 R_{\rm g}$). By comparing the predicted SED at each of these energy dissipation sites to the observed SED, we can provide an observational constraint on $Z_{\rm diss}$.

[9] In the case of silicate dust the radius increases by a factor of ≈1.6 compared with the value we quote here for graphite dust.

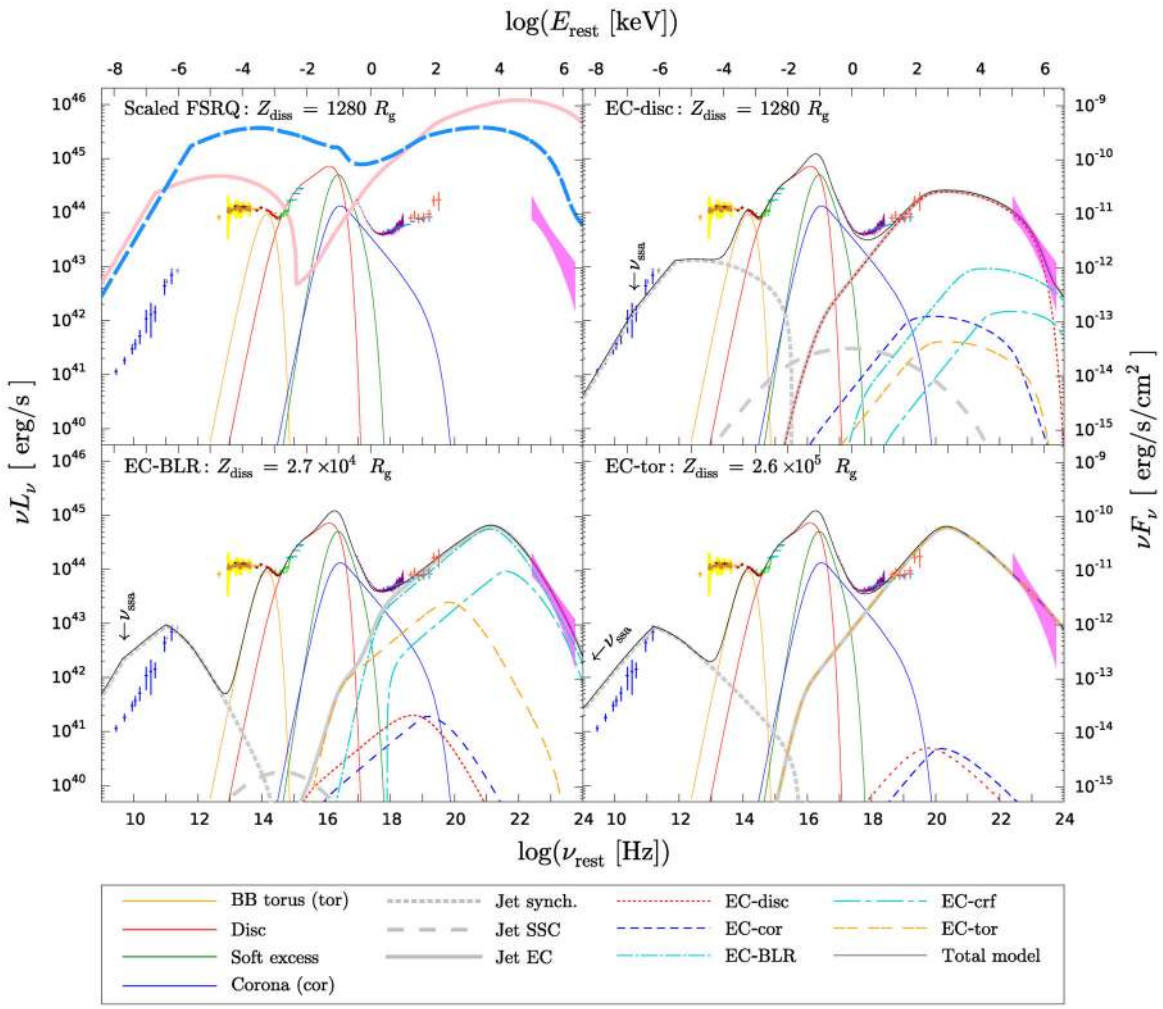

Figure 8. SED fits to radio to γ-ray data with the jet dissipation region at increasing distance Z_{diss} from the BH. The model parameters are given in Table 7. In the top left-hand panel the blue-dashed line shows the total jet plus accretion flow emission corresponding to the scaled FSRQ model; the pink solid line shows a typical high-mass FSRQ jet scaled down in luminosity by a factor of 10. We show the three components of the jet emission (synchrotron, synchrotron self-Compton 'SSC', and external Compton 'EC') as grey lines. The individual EC components (from the disc, corona, BLR, reflection of the corona off the BLR 'crf' and torus) are shown as coloured dotted and dashed lines. Note that the jet emission code does not calculate the radio spectrum below the synchrotron self-absorption frequency ν_{ssa} indicated; here we have extended the radio emission to lower frequencies for illustrative purposes. We do not model the far- or mid-IR data since we attribute this emission to the cool dusty torus; our model here includes emission from the hot dust only. The data are colour-coded the same as in Fig. 1; see Section 2 in the text for a description of the data.

4.2.3 Constraints on input jet model parameters

Whilst Z_{diss} is a priori unknown, we are able to fix or limit the range of several model parameters on observational or physical grounds; these are listed in Table 6.

The external photon field: The parameters of the external photon field are fixed to those we measured or derived from our zero spin plus jet model in Section 4.1.

The jet parameters: The jet viewing angle towards 1H 0323+342 was recently determined from Very Long Baseline Array (VLBA) monitoring by Fuhrmann et al. (2016a). They analysed VLBA radio images taken on several occasions between 2010 October and 2013 July. Several components in the jet had apparent velocities up to $\beta \sim 7$. Using this information, the authors estimated that the jet is aligned at an angle $i \leq 4$–13° to our line of sight. If we make the reasonable assumption of $i = 1/\Gamma_{BLF}$, this also gives us a bulk Lorentz factor $\Gamma_{BLF} \geq 4.4$–14.3, which is consistent with the $\langle\Gamma_{BLF}\rangle = 13$ for FSRQs determined by G10.

To produce the observed SED slope at radio frequencies, we require the sychrotron self-absorption frequency $\nu_{ssa} \gtrsim 10^{11}$ Hz. For $R_{diss} = \phi Z_{diss}$, the synchrotron self-absorption frequency

$$\nu_{ssa} = \left(4.62 \times 10^{14} K B^{5/2} \frac{\phi Z_{diss}}{0.7}\right)^{2/7}, \quad (4)$$

where K is the normalization of the particle distribution. So the dominant factor governing ν_{ssa} is the magnetic field B, with $\nu_{ssa} \propto B^{5/7}$. The luminosity of the synchrotron peak depends on the magnetic field as $L_{synch} \propto B^2$. We require that the synchrotron emission does not contribute substantially to the IR part of the SED as defined by the *Spitzer* and the *WISE* data, which we attribute to thermal emission from the extended dusty torus. The magnetic field must therefore be strong enough to result in a suitably high ν_{ssa}, but not so strong that the synchrotron emission dominates in the IR.

The position and shape of the two jet emission peaks are influenced by the shape of the accelerated electron distribution. We adopt as initial values the mean FSRQ values of Lorentz factors

Table 6. Constraints on jet model parameters.

Param.	Value	Constraint	Ref.
$M_{\rm BH}$	$=2\times10^7$ M$_\odot$	Our mass estimate	[1]
z	=0.0625	NIR / opt. narrow lines	[1]
$R_{\rm in,\,cor}$	$=24.3\,R_{\rm g}$	Accretion disc fitting	[Section 4.1.1]
$R_{\rm out}$	$=2440\,R_{\rm g}$	Accretion disc fitting	[Section 4.1.1]
$\log(L_{\rm cor})$	=44.54 erg s^{-1}	Accretion disc fitting	[Section 4.1.1]
$\Gamma_{\rm cor}$	=2.70	Accretion disc fitting	[Section 4.1.1]
$E_{\rm cor}^{\rm cut}$	=150 keV	Power-law cut-off	[2]
$\log(L_{\rm BLR})$	=43.33 erg s^{-1}	Scaled from $L_{\rm H\,\alpha,\,H\,\beta}$	[Section 4.1.2]
$R_{\rm BLR}$	$=2.72\times10^4\,R_{\rm g}$	Scaled from $L_{1\,\mu{\rm m},5100\text{Å}}$	[Section 4.1.2]
$\log(L_{\rm tor})$	=44.10 erg s^{-1}	Accretion disc fitting	[Section 4.1.3]
$R_{\rm tor}$	$=2.63\times10^5\,R_{\rm g}$	Dust sublimation radius	[Section 4.1.3]
$T_{\rm tor}$	=1730 K	Accretion disc fitting	[Section 4.1.3]
i	$\lesssim$4–13°	Radio jet kinematics	[3]
$\Gamma_{\rm BLF}$	$\gtrsim$4.4–14.3	$i=1/\Gamma_{\rm BLF}$	[3]
ϕ	=0.1 radians	Jet opening angle	[2]
B	≈2.6	⟨FSRQ⟩ value	[2]
$\gamma_{\rm min}$	=1	⟨FSRQ⟩ value	[2]
$\gamma_{\rm brk}$	≈300	⟨FSRQ⟩ value	[2]
$\gamma_{\rm max}$	≈3000	⟨FSRQ⟩ value	[2]
s_1	≈1	⟨FSRQ⟩ value	[2]
s_2	≈2.7	⟨FSRQ⟩ value	[2]
$P_{\rm j}$	$\lesssim 10\,L_{\rm AD}$	Typical jet power	[4]
$U_{\rm e}/U_B$	≈1	Equipartition	[5]

References: [1] Landt et al. (2017); [2] G10; [3] Fuhrmann et al. (2016a); [4] Ghisellini et al. (2014); [5] Dermer et al. (2014). $E_{\rm cor}^{\rm cut}$ is the high-energy cut-off of the coronal power-law; other parameters are described in Sections 4.1.1 and 4.2 of the text.

γ and slopes s from G10. We leave $\gamma_{\rm min}$ fixed to 1 and note that the value of $\gamma_{\rm max}$ does not generally affect the shape of our SED substantially.

The principle of energy equipartition: The lowest-energy solution to jet emission requires that the electron and magnetic field energy densities are approximately equal, i.e. $U_{\rm e}/U_B\approx1$, (see e.g. Dermer et al. 2014). These quantities are not input parameters to the code, but they are calculated as outputs which can then be used as a check of how physically reasonable our models are. This ratio of energy densities can be tuned if necessary by adjusting the parameters $P_{\rm rel}$, B, and $\Gamma_{\rm BLF}$.

4.3 Jet emission models

The full SED includes low-energy data from Effeleberg/IRAM and *Planck* and high-energy data from *Swift* BAT and *Fermi*, in addition to the mid-energy data we modelled in detail in Section 4.1. We then fit an FSRQ-like jet to our data and determine if the jet parameters we obtain are within the range found for the modelled EC emission of other blazars. Our approach to this question is different from the previous work. Whilst other studies of 1H 0323+342 have fit its SED including a jet (Paliya et al. 2014; Yao et al. 2015a), they made a number of assumptions about the external photon field. We apply the model BBODY+OPTXCONV+JET, tying together the parameters $M_{\rm BH}$, $L/L_{\rm Edd}$, i, the comoving distance $D_{\rm c}$ and z between OPTXCONV and JET. Unlike Section 4.1.1, i is not fixed to zero, but is set to be the inverse of the bulk Lorentz factor.

One might expect that the jet power $P_{\rm j}$ to scale with the BH mass and mass accretion rate such that $P_{\rm j}\propto\dot{m}M_{\rm BH}$ where $\dot{m}=\dot{M}/\dot{M}_{\rm Edd}$. Following Gardner & Done (2018), we can determine $Z_{\rm diss}$, $P_{\rm rel}$, and B by appropriately scaling the mean FSRQ values presented by G10.

Table 7. Jet parameters obtained from spectral fits to the full multiwavelength SED with BBODY+OPTXCONV+JET models.

Parameter	Units	Model value			
		Scaled	EC-disc	EC-BLR	EC-tor
$Z_{\rm diss}$	($R_{\rm g}$)	1280	1280	2.7×10^4	2.6×10^5
$Z_{\rm diss}$	(ld)	1.5	1.5	30	300
$a_\star$		0.0	0.0	0.0	0.0
i	(deg)	4.41	4.77	4.98	4.98
$\Gamma_{\rm BLF}$		13.0	12.0	11.5	11.5
δ		13.0	12.0	11.5	11.5
B	(G)	38.0	8.00	0.75	0.15
$\gamma_{\rm min}$		1.00	1.00	1.00	1.00
$\gamma_{\rm brk}$		300	300	150	300
$\gamma_{\rm max}$		3000	3000	3000	30000
$\gamma_{\rm cool}$		19	47	58	163
s_1		1.00	1.50	2.00	1.50
s_2		2.70	2.70	4.25	3.20
$\log(\nu_{\rm ssa})$	(Hz)	11.6	10.6	9.67	8.76
$\log\left(\nu_{\rm peak}^{\rm sync}\right)$	(Hz)	13.8	12.5	11.0	11.2
$\log\left(\nu L_{\nu_{\rm peak}}^{\rm sync}\right)$	(erg s^{-1})	45.56	43.12	42.96	42.92
$\log(P_{\rm rel})$	(erg s^{-1})	42.24	41.00	41.80	41.50
$\log(P_{\rm rad})$	(erg s^{-1})	43.95	42.51	42.76	42.74
$\log(P_{\rm e})$	(erg s^{-1})	43.76	42.74	43.53	43.23
$\log(P_B)$	(erg s^{-1})	44.12	42.70	43.25	43.82
$\log(P_{\rm p})$	(erg s^{-1})	45.91	45.01	46.14	45.32
$\log(P_{\rm j})$	(erg s^{-1})	45.93	45.01	46.14	45.34
$P_{\rm j}/L_{\rm AD}$		4.3	0.52	6.9	1.1
$U_{\rm e}/U_B$		0.44	1.1	1.9	0.26

Notes. Parameters are described in Sections 4.2.1 and 4.3 of the text.

For the other jet parameters, we adopt the mean value $\Gamma_{\rm BLF}=13$ and ⟨FSRQ⟩ values for the electron distribution given in Table 6. Applying this appropriately scaled FSRQ jet to our external photon field gives us the scaled FSRQ model, shown as the blue line in the top-left panel of Fig. 8 and the parameters of which are given in Table 7. This predicted SED is very flat because $B\propto(\dot{m}/M_{\rm BH})^{1/2}$ so the magnetic field for a low-mass high accretion rate object is very high (here $B=38$ G) and synchrotron cooling is highly efficient, resulting in an SED with low Compton dominance.

The product of $\dot{m}$ and $M_{\rm BH}$ we determine for 1H 0323+342 is a factor of 10 lower than that for the average $M_{\rm BH}=10^9$, $\dot{m}=0.1$ FSRQ presented in G10. Simply scaling down the average FSRQ SED by a factor of 10 produces the pink line shown in the same plot. It is immediately apparent that whilst the product $\dot{m}M_{\rm BH}$ for 1H 0323+342 is an order of magnitude lower than that of a standard FSRQ, its jet luminosity is at least *another* order of magnitude lower than these scalings predict.

In the EC-disc model we keep $Z_{\rm diss}=1280\,R_{\rm g}$ (the same value as in the standard scaled models); as can be seen in Fig. 8, at this location it is the disc photons which are upscattered into the Compton hump. However, we adjust the other parameters so as to produce the best fit to the observed SED. It is clear that it has been necessary to reduce B and $P_{\rm rel}$ dramatically compared with the scaled FSRQ model. As a result, the total jet power $P_{\rm j}$ is approximately an order of magnitude lower than predicted by the scaling and in this model it is approximately half the accretion disc luminosity. To find a near-equipartion solution, it has been necessary to reduce the $\Gamma_{\rm BLF}$ slightly to 12, but in doing so we can achieve $U_{\rm e}/U_B=1.1$. The slope s_1 has been increased slightly to better match the shape of the SED but the other parameters defining the accelerated electron distribution are the same. In this model the γ-rays are produced by

the upscattering of accretion disc photons, with a minor contribution from BLR photons at the hardest γ-ray energies. The model reproduces the observed jet emission at both low and high frequencies reasonably well.

In the EC-BLR model the dissipation region has been set to $Z_{\rm diss} = 2.7 \times 10^4\ R_{\rm g}$, just inside of the BLR radius where seed photons from the BLR are responsible for the majority of the γ-ray emission. The parameters of the accelerated electron distribution have been changed more significantly than in the EC-disc model to match the shape of the high-energy part of the SED. However, the synchrotron component of this model now vastly overpredicts the observed radio emission. This is partly a consequence of increasing $Z_{\rm diss}$, which increases the size of the dissipation region and thus reduces the energy density and lowers $\nu_{\rm ssa}$. If we wish to match the high-frequency radio data in flux, we overpredict that at lower frequencies.

The dissipation region in the EC-tor model is set to $Z_{\rm diss} = 2.6 \times 10^5\ R_{\rm g}$, just inside of the hot dust radius. The BLR emission seen by the jet is now strongly de-boosted and the distance from the BH is so great that the energy density of disc and corona seed photons is also very low. At this distance the seed photons from the torus are, in effect, solely responsible for the observed γ-ray and hard X-ray emission. In the EC-tor model even with a relatively low B and high $P_{\rm rel}$, the ratio of $U_{\rm e}/U_B = 0.26$. Because the jet is upscattering low-frequency photons from the torus, it is necessary to increase $\gamma_{\rm max}$ to produce the observed γ-rays. This EC-tor model also overpredicts the observed radio emission.

In summary, we conclude that the dissipation region must be located well within $R_{\rm BLR}$.

5 DISCUSSION

5.1 Is 1H 0323+342 a typical NLS1?

The 2–10 keV photon indices of NLS1s are generally soft ($\langle\Gamma\rangle_{\rm NLS1} = 2.19 \pm 0.10$; Leighly 1999), whereas that of 1H 0323+342 is much harder ($\Gamma_{2-10\,\rm keV} = 1.7$). The X-ray RMS spectrum of the fast variability shows a clear break at ≈1 keV. At least two spectral components are therefore required to fit the *XMM–Newton* EPIC spectra. Landt et al. (2017) did not find such clear evidence for multiple spectral components in their analysis of *Swift* XRT data. Curvature in the X-ray spectrum was only apparent in the co-added spectrum of three *Swift* observations. Here, the higher quality of X-ray data obtained from a long *XMM–Newton* observation affords us a better opportunity for a more detailed spectral decomposition. However, some degeneracy between spectral models still remains, as was discussed in Section 4.1.1, where we presented energy-conserving, physical models of the X-ray spectra.

Previous studies have attempted to determine the BH spin of 1H 0323+342 by fitting a blurred reflection model to X-ray spectral data, but the results are not conclusive. Paliya et al. (2014) found a high spin with $a_\star = 0.96 \pm 0.14$ by modelling *Swift* XRT and BAT data, whereas Yao et al. (2015a) found an upper limit of $a_\star < 0.13$ using *Suzaku* data of a more limited energy range. We explored models which included the effects of BH spin in Section 4.1.1. Both zero spin models provide reasonably good fits to the data, but the high spin model overpredicted the soft X-ray power. Our modelling is therefore suggestive of a low BH spin scenario for 1H 0323+342. However, our model makes a number of assumptions which, if relaxed, could in principle allow for a higher BH spin. The model is energy-conserving and assumes that the accretion power passing through the outer and inner discs is equal. This would not be the case if some power were lost as e.g. as disc wind or transported up the jet itself (Blandford & Payne 1982). A recent well-studied example where this may be the case is the super-Eddington AGN RX J0439.6-5311 (Jin et al. 2017b; Jin, Done & Ward 2017a). A larger BH mass could also allow for a higher spin. Here, we fixed the mass to the value $M_{\rm BH} = 2 \times 10^7\ {\rm M}_\odot$ determined by Landt et al. (2017) from measurements of the hydrogen Balmer and Paschen lines. However, there is emerging evidence (from e.g. accretion disc peak fitting, Calderone et al. 2013; spectropolarimetry, Baldi et al. 2016; and the $M_{\rm BH}$-$L_{\rm bulge}$ relation, D'Ammando et al. 2017) that the BH masses of NLS1s are underestimated when using the standard single-epoch virial methods. These studies have found NLS1 BH masses more in line with the rest of the RL-AGN population with $M_{\rm BH} \geq 10^8\ {\rm M}_\odot$. In the case of this source, the 2-month reverberation mapping study of 1H 0323+342 by Wang et al. (2016) also found a similarly low BH mass of $\left(3.4^{+0.9}_{-0.6}\right) \times 10^7\ {\rm M}_\odot$, so at present there is no strong evidence that the BH mass of 1H 0323+342 is substantially greater than the value we have used. Our model also assumes that the accretion flow is not disrupted by the launching and presence of the powerful relativistic jet.

When modelling the *XMM-Newton* X-ray spectra, we allowed the Galactic column to be a free parameter and found the best fits required an excess of Galactic column density of about 50 per cent above the D&L90 value. Whilst the modelled value is more similar to the total column quoted by Willingale et al. (2013), we consider that it is unlikely that the Galactic column is in fact as high as our models determine since we found no evidence for the additional absorption in the *XMM–Newton* RGS spectrum or our optical and UV data (see the Appendix for further details). However, it is well established that NLS1s commonly exhibit complex intrinsic absorption (e.g. Komossa 2000) and emission (e.g. Smith, Page & Branduardi-Raymont 2008) features. We tested several possibilities including neutral or ionized intrinsic absorption, and *ad hoc* absorption and emission features following Gallo et al. (2004) but these did not make as great an improvement in the fit as the increased neutral Galactic column or 'correct' the shape of the deabsorbed spectrum. We have adopted the increased Galactic column as the simplest solution in our models which corrects the spectral shape and gives the greatest improvement in the fit statistic. Doing so does not substantially change the main conclusions from our subsequent SED modelling. However, if we do not allow for this additional absorbing column, then we are unable to include a soft Comptonization region in the models presented in Section 4.1.1. Consequently, the corona photon index is slightly harder and the accretion disc emission increases by a factor of ≈1.4 compared with our zero spin plus jet model. Nevertheless, these changes are not significant enough to basically alter our jet modelling or conclusions.

Apart from its jet, there is nothing we have found here that sets 1H 0323+342 apart from other NLS1s; its mass and Eddington ratio are both only slightly higher than the average values reported by Rakshit et al. (2017). Our extensive exploration of the modelling parameter space shows that the IR-to-X-ray SED of 1H 0323+342 is within the range observed for NLS1s, but with the addition of a jet component. Why this particular NLS1 possesses a relativistic jet when the vast majority of others do not therefore remains an open question.

5.2 Contribution of the jet to the IR and X-ray emission

Turning to a much lower-frequency part of the SED, our *Spitzer* IRS spectrum is shown in Fig. 2. It can been seen in the figure

that the *WISE* photometry agrees well with our *Spitzer* data despite the former being taken approximately 18 months later, indicating very little, if any, variability over a time-scale of years. In the *Spitzer* IRS spectrum, we can see two strong, broad humps at ≈11 and 18 μm which we attribute to the 9.7 and 18 μm silicate features commonly seen in emission in type 1 AGN spectra. The 9.7 μm feature is often not observed at the rest-frame wavelength 9.7 μm, but redward of this position. The apparent redshift of this feature was seen in all of the *Spitzer* spectra of a sample of 12 RL-AGNs studied by Landt, Buchanan & Barmby (2010), and had previously been seen in a few other sources (e.g. Siebenmorgen et al. 2005; Sturm et al. 2005; Schweitzer et al. 2008) but its cause is currently unknown. Some weak polycyclic aromatic hydrocarbon (PAH) features may also be present in the spectrum. Since we do not see a featureless continuum or flux variability which we would expect from synchrotron emission, these features suggest that most of this mid/far-IR emission originates from the torus rather than from the jet. This interpretation is contrary to that of others (Abdo et al. 2009b; Paliya et al. 2014; Yao et al. 2015a) who have studied this object and attributed the IR emission to the jet synchrotron component. As a consequence, our jet models have a lower-luminosity synchrotron peak and higher Compton dominance in the SED.

In Section 2.2.1 we measured the flux and hence the luminosity of the mid-IR emission line [O IV] λ25.89 μm. We compared the luminosity of the line to the X-ray luminosities in the *XMM–Newton* and *Swift* BAT bands. Using the derived luminosity of [O IV], $\log(L_{[\mathrm{O\,IV}]}) = 41.3$, and the 2–10 keV X-ray luminosity, $\log(L_{2-10\,\mathrm{keV}}) = 43.9$, we can compare these values with those of the sample of AGNs studied by Diamond-Stanic, Rieke & Rigby (2009); we see that 1H 0323+342 is broadly consistent with other Seyfert 1s shown in their Fig. 4. However, if we now look at the corresponding relation between the hard X-rays and [O IV] (e.g. LaMassa et al. 2010, their fig. 8), we see that 1H 0323+342, having $\log(L_{14-195\,\mathrm{keV}}) = 44.45 \pm 0.05$, lies above the correlation, suggesting that it is more luminous in hard X-rays by a factor of about 5 with respect to the other Seyfert 1 AGN in their sample. The detection of the [O IV] line is clearly of limited significance, given the S/N of the *Spitzer* IRS spectrum. If instead we treat the measured flux as an upper limit, then 1H 0323+342 must be even more overluminous in 14–195 keV X-rays, in terms of the correlation found for other AGNs. This excess of hard X-ray luminosity supports our preference for a model in which emission from the relativistic jet makes a contribution to the hard X-rays.

In Section 3.2.2 we show that the continuum fit to the X-ray spectrum is improved if we add a narrow-line feature at 6.43 keV with EW = 36 ± 8 eV, which we associate with neutral Fe Kα. For comparison, Shu, Yaqoob & Wang (2010) measured the EWs of the narrow cores of Fe Kα in a sample of Seyfert AGNs observed by *Chandra*, finding $\langle \mathrm{EW} \rangle = 53 \pm 3$ eV. In RL AGNs, the contribution to the X-ray continuum of Doppler-boosted emission from the jet will result in a relative weakness (of the EW, by dilution from the additional continuum flux) of the fluorescent Fe Kα emission line. Bianchi et al. (2007) derived a relationship between the EW of the narrow Fe Kα and the 2–10 keV luminosity based on RQ type 1 AGN (equation (1) in their paper). From this relation, we can estimate that the narrow Fe Kα EW should be ≈56 eV if 1H 0323+342 were RQ and the jet made no contribution to the 2–10 keV continuum. The lower EW we have determined tentatively suggests that some jet emission may be present in the *XMM–Newton* bandpass.

5.3 The external photon field

Our new approach here was to use the wealth of quasi-simultaneous spectroscopy and photometry to derive the seed photons for the external Compton components input into the jet code. This is clearly a better approach than assuming a given SED shape, especially given our well-sampled SED.

The accretion disc luminosity (consequently the Eddington ratio) we determine from our zero spin plus jet model actually agrees very well with the values we would obtain from estimating the mass accretion rate $\dot{M}$ from the optical luminosity (Davis & Laor 2011) and assuming $\eta = 6$ per cent to calculate the bolometric luminosity from $L = \eta \dot{M} c^2$. The agreement of these values with our zero spin plus jet SED model lends some support to this model over the high-spin case model where the Eddington ratio and disc luminosity were both higher. In the G&T09 model, the corona extends out to 60 R_{g} and has one tenth of the accretion disc luminosity. As can be seen from Table 5, our corona is more luminous but more compact than this, extending to 24 R_{g}. The corona photon index in the G&T09 model is assumed to be 2 whereas the values we determined are much softer at 3.59 in Sections 3.2.1 and 2.7 in the zero spin plus jet model. Despite being more luminous than the standard model assumes, the EC-corona emission is not a very strong component in any of our models. The JET model is insensitive to subtle changes in the spectral shape and geometry of the corona so the difference in photon indices and radii also have very little impact on our results. G&T09 scale the BLR luminosity and radius from the accretion disc luminosity. Table 5 shows that their standard assumptions predict a larger and much more luminous BLR than we determined in Section 4.1.2. The smaller radius we determine is in better agreement with the value obtained from the reverberation mapping study of Wang et al. (2016). Interestingly, our value for the BLR luminosity is a factor of 10 lower than the G&T09 model assumption that it is one tenth of the accretion disc luminosity. The BLR radius that we determine is just over half of the value calculated in the standard model. However, the energy density of BLR seed photons is $U'_{\mathrm{BLR}} \propto L_{\mathrm{AD}}$ and $U'_{\mathrm{BLR}} \propto R_{\mathrm{BLR}}^{-2}$, so the overall difference in U'_{BLR} is a factor ≈3, which does not substantially change our conclusions.

The torus we adopt is smaller and less bright than the standard model assumes. Our IR spectrum only samples emission from the hottest dust on the inner edge of the torus, so the temperature we determine from our models is much greater than that in the G&T09 prescription which characterizes the dust as much cooler and more extended. Of course, both are simplifications of the actual torus temperature-radius and luminosity-radius profiles. Had we used the standard assumptions with an energy density U'_{tor} smaller by a factor ≈5, the torus component in the EC-BLR model would be weaker. The dissipation region in our EC-tor model would have been placed even further out, so v_{ssa} would be smaller and the model would still overpredict the radio emission.

5.4 The impact of variability

We have reason to claim that the non-simultaneity of our broad-band data does not strongly affect our results and conclusions. The *XMM-Newton* optical/UV photometry and X-ray spectra are truly simultaneous and sample the outer and inner accretion flows, respectively. The high-frequency end of the *XMM-Newton* spectra and low-frequency end of the *NuSTAR* spectra are of very similar flux levels despite the 17-month gap between observations. As noted in Section 4.1.1, the apparent discrepancy in spectral shape

may be due to a calibration issue. Considering the higher frequencies, the flux levels of the *NuSTAR* and *Swift* BAT X-ray spectra are consistent in their region of overlap and the *Fermi* γ-ray data were chosen to sample the period covering the *XMM–Newton* observation. Turning to lower frequencies, the *XMM–Newton* optical photometry (simultaneous with the X-rays) are consistent with points sampling the continuum determined from the Keck optical spectrum. The GNIRS spectrum was flux-scaled to match the Keck data, because we suspect that the apparent difference in flux is due to a shift resulting from the uncertain absolute flux calibration of the near-IR spectrum rather than genuine source variability (as described in Landt et al. 2017). After this correction has been applied, the near-IR data then appear to connect with the mid- and far-IR bands sampled by *Spitzer* and *WISE*. As we commented in Section 5.2, the *WISE* photometry agrees very well with the *Spitzer* data even though the observations were separated by more than a year.

With regard to the Effelsberg and IRAM radio data, Angelakis et al. (2015) reported flux density variability magnitudes on average ≈30 per cent and up to 63 per cent, with the variability being more pronounced at higher frequencies. Whilst the flux densities at lower frequencies were generally stable, frequencies 14.6 GHz and above exhibited occasional flaring. However, the mean values from which we used in our analysis are not strongly affected by the flaring episodes and are broadly consistent with the stable, baseline level.

We noted in Sections 2.3.3 and 3.1.2 and that the X-ray and γ-ray data were obtained during periods of low activity. Given the constancy in flux betweeen neighbouring frequency bands, it is therefore reasonable to conclude that all of our multiwavelength data are appropriate to describe this source in a low state. Although our data are mostly not simultaneous, for the reasons given above we do not expect that this impairs our overall conclusions.

5.5 The origin of the γ-ray emission

It is generally accepted that in the case of a high-accretion rate blazar, such as 1H 0323+342, the γ-ray emission from 1H 0323+342 results from the EC process. Here we compare our general findings with those from other similar studies. Both Abdo et al. (2009b) and Paliya et al. (2014) (for the quiescent state) found that the dissipation region must be relatively near to the BH, with $Z_{\rm diss} \approx 1300\,R_{\rm g}$, very similar to the value we used in the EC-disc model here, which adopts the mean FSRQ $Z_{\rm diss}$ of G10. Yao et al. (2015a) were unable to constrain the location so well, since models with a dissipation region located inside or outside of the BLR both reproduced their broad-band SED reasonably well. In our preferred EC-disc model, the jet emission region appears to be relatively near the accretion disc, with EC-disc photons producing the hard X-rays and the γ-rays. This is different from the findings of Paliya et al. (2014) where EC-BLR photons were dominant in all states (both quiescent and flaring). This is also different to Yao et al. (2015a), who considered only EC-BLR and EC-torus situations. Here, both the EC-BLR and EC-tor models are shown to overpredict the observed radio emission.

In many jet models, such as ours, it is assumed that $R_{\rm diss} = \phi Z_{\rm diss}$, therefore a compact emission region (with small $R_{\rm diss}$) must be relatively near to the core of the AGN. However, other geometries have been proposed such as the 'spine-sheath' (e.g. Sol, Pelletier & Asseo 1989; Ghisellini, Tavecchio & Chiaberge 2005; Sikora, Rutkowski & Begelman 2016) or 'turbulent cell' (e.g. Marscher & Jorstad 2010) models. In these cases, the jet does not radiate across its entire cross-section so a compact emission region does not necessarily imply one that is close to the BH. For simplicity, and for the ease of comparison with the work of other authors, we have not considered alternative jet geometries here.

Overall, our EC-disc model has a set of parameters that best match the broad-band SED, across an exceptionally wide range of frequencies, from the radio to γ-rays. This model has the added attraction that is very close to an energy equipartition solution with $U_{\rm e}/U_B = 1.1$. The parameters of the accelerated electron distribution for this model are the same as those for the scaled-down FSRQ model, with the exception of the slope s_1 which is 1.5 in the former and 1.0 in the latter. It differs from the scaled FSRQ model mainly in that its magnetic field and power injected into the electrons are much lower than predicted; we discuss this further in the next section.

5.6 Where does 1H 0323+342 lie in the blazar sequence?

Our interpretation of mid-IR emission as being torus-dominated limits the peak luminosity of the synchrotron component and increases the dominance of the EC peak in the SED. We therefore arrive at an SED shape typical of an FSRQ but at a luminosity more like that of a BL Lac. It has been predicted that low-mass, lower-luminosity FSRQs would be detected by *Fermi*, which has a greater sensitivity than its predecessor *EGRET*. However, the blue line in the top-left panel of Fig. 8 shows that a scaled-down FSRQ SED is both more luminous and has a flatter shape more like a BL Lac than is observed. If we simply scale down a typical FSRQ SED by a factor of 10 (the pink line in the top-left panel of Fig. 8), it is also much more luminous than the data although the shape is more similar to the one we fit in the EC-disc model. In both cases the synchrotron and Compton humps in the SED are at frequencies more typical of FSRQs than the 'bluer' SEDs of BL Lacs. The accelerated electron distribution in our EC-disc model has parameters very similar to that of a typical FSRQ; the higher-frequency peaked BL Lacs have much greater $\gamma_{\rm brk}$ and $\gamma_{\rm max}$. Additionally, the bulk Lorentz factor of this model is more similar to that of an FSRQ than a BL Lac (which have $\langle\Gamma_{\rm BLF}\rangle = 15$, G10).

Ghisellini et al. (2014) found a clear positive correlation between the jet and disc powers in a sample of over 200 blazars. As well as this relation, they also found that the jet powers exceeded the accretion disc luminosities typically by a factor of ∼10. Clearly, this is not the case for 1H 0323+342 where the jet power in our EC-disc model is approximately half the disc luminosity. Zero BH spin implies a low radiative efficiency, $\eta = 0.06$, and we can determine that $\log\left(\dot{M}c^2\right) = 46.5$, so 1H 0323+342 lies well outside of the 3σ dispersion of $P_{\rm j}$-$\dot{M}c^2$ determined by Ghisellini et al. (2014). Even if we allow for a high spin (which our energy-conserving models disfavoured) we calculate $\log\left(\dot{M}c^2\right) = 45.8$ and 1H 0323+342 is then only just inside of the 3σ region. We showed in our EC-disc jet model that in order to match the observed SED it is necessary to reduce both $P_{\rm rel}$ and B from the values predicted by the scaled FSRQ model. As well as having a very low jet power for an FSRQ, 1H 0323+342 has a low jet power compared with the prototypical γ-NLS1 PMN J0948+0022, as was noted by both Abdo et al. (2009b) and Paliya et al. (2014). Since the strength of the magnetic field determines how efficiently the jet can extract the rotational energy of the BH, it is possible that the (relatively) weak magnetic field of 1H 0323+342 is less well able to extract spin power and inject it into the jet. Our findings also indicate that it is plausible that 1H 0323+342 has a lower BH spin than other blazars, and consequently is unable to host as powerful a jet.

Table 8. Comparison of 1H 0323+342 jet powers.

Jet model	log ($P_{\rm rad}$) (1)	log ($P_{\rm e}$) (2)	log (P_B) (3)	log ($P_{\rm p}$) (4)	log ($P_{\rm j}$) (5)
EC-disc (5°)	42.51	42.74	42.70	45.01	45.01
EC-disc (3°)	42.18	42.15	42.58	44.44	44.45
Abdo[a]	42.8	42.7	43.3	44.3	44.4
Paliya[b]	41.29			44.06	
Yao[c]	43.9	43.4	42.6	43.7	44.2

Notes. Here we compare the jet powers calculated for our EC-disc model with those of: [a]Abdo et al. (2009b); the quiescent state model of [b]Paliya et al. (2014) and the IC/BLR model of [c]Yao et al. (2015a). In the columns we quote the logarithms of: (1) the radiative power; (2) the power in the bulk motion of electrons; (3) the Poynting power; (4) the power in the bulk motion of protons, and (5) the total jet power, in units erg s^{-1}.

5.7 A comparison of jet powers

We claim that 1H 0323+342 hosts an underpowered jet for an FSRQ, compared with those presented by G10 and Ghisellini et al. (2014). The jet power that is determined is strongly dependent on the assumptions made in the modelling. Other authors have determined the jet power of 1H 0323+342 by fitting a single-zone leptonic jet model to its broad-band SED; we tabulate the relevant values in Table 8. It can be seen that the power that was calculated for our preferred model, 'EC-disc (5°)', is greater than those of these previous studies and here we discuss some of the differences.

The most straightforward comparison is to the model adopted by Abdo et al. (2009b) because they use the most similar modelling prescription to our own. However, they have adopted a BH mass estimate half of our value, so whilst their $R_{\rm diss}$ is equal to ours in mass-scaled units, it is a factor of 2 smaller in absolute terms which affects the calculated energy densities. Another key difference is their use of a smaller inclination angle $i = 3°$ rather than our value of $i = 1/\Gamma_{\rm BLF} \approx 5°$, although they use the same $\Gamma_{\rm BLF} = 12$ as us. The Doppler boosting in their case is therefore greater by a factor of 4 and they can fit the observed γ-ray emission with a jet which is around five times less powerful than ours. We find that we can replicate the shape of our EC-disc SED model at a lower inclination angle of 3° by turning down B and $P_{\rm rel}$, but keeping $\Gamma_{\rm BLF} = 12$. In this case we obtain a jet power very similar to Abdo et al. (2009b), as shown in Table 8.

The quiescent state model of Paliya et al. (2014) has approximately an order of magnitude lower kinetic power than our model. This difference is in part due to their choice of a much lower $\Gamma_{\rm BLF} = 7$; since $P_{\rm p} \propto \Gamma^2_{\rm BLF}$, for the same number of protons the kinetic power would be reduced by a factor ≈0.3.

The IC/BLR model of Yao et al. (2015a) has a very low $\Gamma_{\rm BLF} = 2.7$, therefore the bulk motion of particles is not the dominant factor in the jet power, and the radiative power contributes approximately half of the total jet power. Their injected electron distribution is skewed towards higher Lorentz factors, with $\gamma_{\rm brk} = 1073$ in their case compared with our value of $\gamma_{\rm brk} = 300$. As a result, the power in the bulk motion in protons is only approximately twice the power in the bulk motion in electrons. However, since they do not quote the injected power $P_{\rm rel}$, we are unable to make a more detailed comparison.

This diversity of jet powers illustrates the strong dependence on the modelling assumptions. Since we adopted the same approach as G10, the most appropriate comparison is to their large sample of FSRQs. The models of other authors can fit similar SEDs for this source and they have found even lower jet powers. Therefore, we are confident that our principal conclusion that 1H 0323+342 hosts a low-powered jet remains robust.

6 SUMMARY AND CONCLUSIONS

We assembled a well-sampled and wide-ranging multiwavelength data set including our new IR, optical, and X-ray spectra and supplemented these with archival data including spectra and photometry in other wavebands from radio through to γ-rays. The observations, data reduction, and reference sources were described in Section 2. In Section 3, we performed a temporal and spectral analysis of a long (80 ks) *XMM–Newton* observation. We found evidence for complexity in the low-energy range of the X-ray spectrum which is possibly due to absorption in addition to the Galactic column. The dereddened/deabsorbed IR, optical and X-ray spectra, and optical/UV photometry were used to fit an energy-conserving accretion disc model to our data in Section 4.1.1. The results from this modelling, along with measurements of emission lines observed in our optical spectrum, allowed us to define the photon field in the vicinity of the central engine of 1H 0323+342. In particular, we determined the size scales and luminosities of the accretion disc and its corona, the BLR and the dusty torus. We then introduced these parameters into a relativistic jet emission code to determine the jet parameters which best reproduce the observed SED. The results from our modelling of the jet are presented in Section 4.3.

Our main conclusions are as follows:

(i) It is possible to fit an energy-conserving accretion flow model to the IR-to-X-ray SED in which the accretion flow has parameters typical of a NLS1 and where the jet makes a contribution to the hard X-rays. This is only possible if the BH spin is low or zero; a high BH spin model predicts more energy in soft X-rays than is seen in the data. We find the X-ray emission has contributions from a soft-spectrum corona and a soft Comptonization region with temperature $kT_{\rm e} = 0.22$ keV, and determine a relatively high Eddington ratio of $L/L_{\rm Edd} = 0.6$.

(ii) We detect a weak iron line in the *XMM–Newton* EPIC spectra which has an energy consistent with neutral Fe Kα fluorescence.

(iii) We find that 1H 0323+342 has a broad-band SED with a similar shape to an FSRQ (showing high Compton dominance) but with a similar luminosity to a BL Lac. We show that this source is *not* consistent with being a mini FSRQ, since scaling down standard FSRQ jet parameters by BH mass and mass accretion rate produces an SED model which vastly overpredicts the observed emission. The jet in 1H 0323+342 appears to be underpowered by at least an order of magnitude compared with predictions made by scaling an average FSRQ jet. With respect to the accretion power, the source lies outside of the 3σ dispersion region of the $P_{\rm j}$–$\dot{M}c^2$ relation determined by Ghisellini et al. (2014).

(iv) We show that (within the assumptions of our jet model) the energy dissipation region of the jet must be located near to the BH and well within the BLR radius. In our preferred jet emission model, seed photons from the accretion disc are upscattered to produce the observed γ-ray emission.

Our detailed study of 1H 0323+342 has shed new light on its accretion properties, e.g. the Eddington ratio, the nature of its outflow (jet), the interplay between the relativistic particles and the radiation field and its relation to other blazars. However, this is only one example of the small group of γ-NLS1s, and in-depth studies of a number of other examples need to be made to reveal whether they share similar characteristics or are a heterogeneous sample.

ACKNOWLEDGEMENTS

DK acknowledges the receipt of a Science and Technology Facilities Council studentship (ST/N50404X/1). DK, HL, MJW, CD, and EG acknowledge support from the STFC (ST/L00075X/1). MPS acknowledges support from the STFC through grant ST/N000919/1, the John Fell Oxford University Press (OUP) Research Fund, and the University of Oxford. Thanks goes to both Emanuele Nardini and Filippo D'Ammando for useful discussions regarding the X-ray spectral analysis.

In this paper we have made use of the following:

(i) data from *Fermi*, a NASA mission operated and funded NASA, the U.S. Department of Energy and institutions in France, Germany, Japan, Italy, and Sweden;

(ii) data from *Spitzer*, *WISE*, *Planck*, and 2MASS, which are available from the NASA/IPAC Infrared Science Archive, which is operated by the Jet Propulsion Laboratory, California Institute of Technology, under contract with NASA;

(iii) data from *NuSTAR*, a project led by the California Institute of Technology, managed by the Jet Propulsion Laboratory and funded by NASA;

(iv) data from *Swift*, and its XRT Data Analysis Software (XRTDAS) developed under the responsibility of the ASI Science Data Center (ASDC), Italy;

(v) data from and software developed for *XMM–Newton*, an ESA science mission with instruments and contributions directly funded by ESA Member States and NASA;

(vi) data and software (including the FTOOLS[10]; Blackburn 1995) provided by the High Energy Astrophysics Science Archive Research Center (HEASARC), which is a service of the Astrophysics Science Division at NASA/GSFC and the High Energy Astrophysics Division of the Smithsonian Astrophysical Observatory;

(vii) Ned Wright's cosmology calculator (Wright 2006).

REFERENCES

Abdo A. A. et al., 2009a, ApJ, 699, 976
Abdo A. A. et al., 2009b, ApJ, 707, L142
Abdollahi S. et al., 2017, ApJ, 846, 34
Acero F. et al., 2016, ApJS, 223, 26
Angelakis E. et al., 2015, A&A, 575, A55
Arnaud K. A., 1996, in Jacoby G. H., Barnes J., eds, ASP Conf. Ser. Vol. 101, Astronomical Data Analysis Software and Systems V. Astron. Soc. Pac., San Francisco, p. 17
Atwood W. B. et al., 2009, ApJ, 697, 1071
Baldi R. D., Capetti A., Robinson A., Laor A., Behar E., 2016, MNRAS, 458, L69
Baumgartner W. H., Tueller J., Markwardt C. B., Skinner G. K., Barthelmy S., Mushotzky R. F., Evans P. A., Gehrels N., 2013, ApJS, 207, 19
Ben Bekhti N., Richter P., Winkel B., Kenn F., Westmeier T., 2009, A&A, 503, 483
Bentz M. C. et al., 2013, ApJ, 767, 149
Bianchi S., Guainazzi M., Matt G., Fonseca Bonilla N., 2007, A&A, 467, L19
Blackburn J. K., 1995, in Shaw R. A., Payne H. E., Hayes J. J. E., eds, ASP Conf. Ser. Vol. 77, Astronomical Data Analysis Software and Systems IV. Astron. Soc. Pac., San Francisco, p. 367
Blandford R. D., Payne D. G., 1982, MNRAS, 199, 883
Blandford R. D., Znajek R. L., 1977, MNRAS, 179, 433
Calderone G., Ghisellini G., Colpi M., Dotti M., 2012, MNRAS, 424, 3081
Calderone G., Ghisellini G., Colpi M., Dotti M., 2013, MNRAS, 431, 210
Cardelli J. A., Clayton G. C., Mathis J. S., 1989, ApJ, 345, 245
Carpenter J. M. et al., 2008, ApJS, 179, 423
Celotti A., Padovani P., Ghisellini G., 1997, MNRAS, 286, 415
D'Ammando F., Orienti M., Larsson J., Giroletti M., 2015, MNRAS, 452, 520
D'Ammando F., Orienti M., Finke J., Larsson J., Giroletti M., Raiteri C., 2016, Galaxies, 4, 11
D'Ammando F., Acosta-Pulido J. A., Capetti A., Raiteri C. M., Baldi R. D., Orienti M., Ramos Almeida C., 2017, MNRAS, 469, L11
Davis S. W., Laor A., 2011, ApJ, 728, 98
Dermer C. D., Cerruti M., Lott B., Boisson C., Zech A., 2014, ApJ, 782, 82
Diamond-Stanic A. M., Rieke G. H., Rigby J. R., 2009, ApJ, 698, 623
Dickey J. M., Lockman F. J., 1990, ARA&A, 28, 215 (D&L90)
Donato D., Perkins J. S., 2011, Astron. Telegram, 3452
Done C., Davis S. W., Jin C., Blaes O., Ward M., 2012, MNRAS, 420, 1848
Done C., Jin C., Middleton M., Ward M., 2013, MNRAS, 434, 1955
Falomo R., Kotilainen J. K., Carangelo N., Treves A., 2003, ApJ, 595, 624
Foschini L., 2011, Proc. Sci., Evidence of Powerful Relativistic Jets in Narrow-Line Seyfert 1 Galaxies. SISSA, Trieste, PoS(NLS1)024
Fossati G., Maraschi L., Celotti A., Comastri A., Ghisellini G., 1998, MNRAS, 299, 433
Francis P. J., Hewett P. C., Foltz C. B., Chaffee F. H., Weymann R. J., Morris S. L., 1991, ApJ, 373, 465
Fuhrmann L. et al., 2016a, Res. Astron. Astrophys., 16, 176
Fuhrmann L. et al., 2016b, A&A, 596, A45
Gallo L. C., Boller T., Brandt W. N., Fabian A. C., Vaughan S., 2004, A&A, 417, 29
Gardner E., Done C., 2018, MNRAS, 473, 2639
Gaskell C. M., Shields G. A., Wampler E. J., 1981, ApJ, 249, 443
Ghisellini G., Tavecchio F., 2009, MNRAS, 397, 985 (G&T09)
Ghisellini G., Tavecchio F., 2015, MNRAS, 448, 1060
Ghisellini G., Tavecchio F., Chiaberge M., 2005, A&A, 432, 401
Ghisellini G., Maraschi L., Tavecchio F., 2009, MNRAS, 396, L105
Ghisellini G., Tavecchio F., Foschini L., Ghirlanda G., Maraschi L., Celotti A., 2010, MNRAS, 402, 497 (G10)
Ghisellini G., Tavecchio F., Maraschi L., Celotti A., Sbarrato T., 2014, Nature, 515, 376
Ghisellini G., Righi C., Costamante L., Tavecchio F., 2017, MNRAS, 469, 255
Gierliński M., Done C., 2004, MNRAS, 349, L7
Ho L. C., 2002, ApJ, 564, 120
Ingram A., van der Klis M., Middleton M., Altamirano D., Uttley P., 2017, MNRAS, 464, 2979
Jansen F. et al., 2001, A&A, 365, L1
Jin C., Ward M., Done C., Gelbord J., 2012, MNRAS, 420, 1825
Jin C., Done C., Ward M., 2017a, MNRAS, 468, 3663
Jin C., Done C., Ward M., Gardner E., 2017b, MNRAS, 471, 706
Komossa S., 2000, New A Rev., 44, 483
Komossa S., Voges W., Xu D., Mathur S., Adorf H.-M., Lemson G., Duschl W. J., Grupe D., 2006, AJ, 132, 531
LaMassa S. M., Heckman T. M., Ptak A., Martins L., Wild V., Sonnentrucker P., 2010, ApJ, 720, 786
Landt H., Buchanan C. L., Barmby P., 2010, MNRAS, 408, 1982
Landt H., Bentz M. C., Peterson B. M., Elvis M., Ward M. J., Korista K. T., Karovska M., 2011, MNRAS, 413, L106
Landt H., Ward M. J., Peterson B. M., Bentz M. C., Elvis M., Korista K. T., Karovska M., 2013, MNRAS, 432, 113
Landt H. et al., 2017, MNRAS, 464, 2565
Laor A., 2000, ApJ, 543, L111
Leighly K. M., 1999, ApJS, 125, 317
Madejski G., Sikora M., 2016, ARA&A, 54, 725
Marscher A. P., Jorstad S. G., 2010, preprint (arXiv:1005.5551)
Martin D. C. et al., 2005, ApJ, 619, L1
McLure R. J., Dunlop J. S., 2001, MNRAS, 327, 199
Middelberg E. et al., 2004, A&A, 417, 925
Mor R., Netzer H., 2012, MNRAS, 420, 526

[10] http://heasarc.gsfc.nasa.gov/ftools/

Moretti A. et al., 2005, in Siegmund O. H. W., ed., Proc. SPIE Conf. Ser. Vol. 5898, UV, X-Ray, and Gamma-Ray Space Instrumentation for Astronomy XIV. SPIE, Bellingham, p. 360
Osterbrock D. E., Pogge R. W., 1985, ApJ, 297, 166
Paliya V. S., Sahayanathan S., Parker M. L., Fabian A. C., Stalin C. S., Anjum A., Pandey S. B., 2014, ApJ, 789, 143
Planck Collaboration XXVI, 2016, A&A, 594, A26
Plotkin R. M., Markoff S., Trager S. C., Anderson S. F., 2011, MNRAS, 413, 805
Porquet D., Reeves J. N., O'Brien P., Brinkmann W., 2004, A&A, 422, 85
Poznanski D., Prochaska J. X., Bloom J. S., 2012, MNRAS, 426, 1465
Rakshit S., Stalin C. S., Chand H., Zhang X.-G., 2017, ApJS, 229, 39
Risaliti G., 2007, in Ho L. C., Wang J.-W., eds, ASP Conf. Ser. Vol. 373, The Central Engine of Active Galactic Nuclei. Astron. Soc. Pac., San Francisco, p. 458
Schweitzer M. et al., 2008, ApJ, 679, 101
Shakura N. I., Sunyaev R. A., 1973, A&A, 24, 337
Shu X. W., Yaqoob T., Wang J. X., 2010, ApJS, 187, 581
Siebenmorgen R., Haas M., Krügel E., Schulz B., 2005, A&A, 436, L5
Sikora M., Begelman M. C., 2013, ApJ, 764, L24
Sikora M., Begelman M. C., Rees M. J., 1994, ApJ, 421, 153
Sikora M., Rutkowski M., Begelman M. C., 2016, MNRAS, 457, 1352
Skrutskie M. F. et al., 2006, AJ, 131, 1163
Smith J. D. T. et al., 2007, PASP, 119, 1133
Smith R. A. N., Page M. J., Branduardi-Raymont G., 2008, A&A, 490, 103
Sol H., Pelletier G., Asseo E., 1989, MNRAS, 237, 411
Sturm E. et al., 2005, ApJ, 629, L21
Wang F. et al., 2016, ApJ, 824, 149
Werner M. W. et al., 2004, ApJS, 154, 1
Willingale R., Starling R. L. C., Beardmore A. P., Tanvir N. R., O'Brien P. T., 2013, MNRAS, 431, 394
Wright E. L., 2006, PASP, 118, 1711
Wright E. L. et al., 2010, AJ, 140, 1868
Yao S., Yuan W., Komossa S., Grupe D., Fuhrmann L., Liu B., 2015a, AJ, 150, 23
Yao S., Yuan W., Zhou H., Komossa S., Zhang J., Qiao E., Liu B., 2015b, MNRAS, 454, L16
Yuan W., Zhou H. Y., Komossa S., Dong X. B., Wang T. G., Lu H. L., Bai J. M., 2008, ApJ, 685, 801
Zhang F., Yu Q., Lu Y., 2017, ApJ, 845, 88
Zheng Y. G., Yang C. Y., Zhang L., Wang J. C., 2017, ApJS, 228, 1

APPENDIX: ADDITIONAL X-RAY ABSORPTION

As stated in Section 3.2.1, if we adopted the D&L90 Galactic column $N_{\rm H}^{\rm Gal} = 1.46 \times 10^{21}$ cm^{-2}, the deabsorbed *XMM–Newton* EPIC X-ray spectra turned down towards lower energies and did not smoothly connect with the OM photometry. We achieved a significant improvement in the fit ($\Delta\chi^2 = 162$ for one additional free parameter), and a corrected shape in the deabsorbed spectra, if we allowed the $N_{\rm H}^{\rm Gal}$ to be a free parameter in our fits and increase to a value $\approx 2.2 \times 10^{21}$ cm^{-2}.

We tested our other X-ray data for evidence of this additional absorption. We added the *Swift* XRT spectra recorded between 2015 August 2 and September 29; the co-added spectrum contains 8724 counts. A sum of two power-laws model with $\Gamma_1 = 2.2^{+0.2}_{-0.1}$ and $\Gamma_2 = 1.0^{+0.3}_{-0.4}$ has $\chi^2_\nu = 357/260 = 1.37$ if the Galactic column is fixed to 1.46×10^{21} cm^{-2}. Allowing the Galactic column to be a free parameter, we find the fit improves by $\Delta\chi^2 = 18$ with an *F*-test probability of 99.97 per cent. The Galactic column in this model is very high at $\left(4.0^{+0.9}_{-0.8}\right) \times 10^{21}$ cm^{-2} and the soft photon index is very steep, $\Gamma_1 = 4.9 \pm 0.7$, but clearly these parameters are poorly constrained by the limited quality of the spectrum. We note that the shapes of the deabsorbed, co-added *Swift* XRT spectra with and without the additional column agree with the corresponding *XMM–Newton* EPIC spectra. We fitted a blackbody plus power-law model fitted to the *XMM–Newton* RGS spectra (taken contemporaneously with the EPIC spectra) and recorded a C-statistic 2138 with the D&L90 value of $N_{\rm H}^{\rm Gal}$. Increasing the Galactic column to 2.1×10^{21} cm^{-2} worsens the C-statistic to 2211. However, we note that above $\approx$30 Å (below $\approx$0.4 keV) the count rates in many channels are consistent with zero. Therefore, there is not such strong evidence for a higher Galactic column in our *Swift* XRT data and no evidence in the *XMM–Newton* RGS spectrum.

It is unlikely that the neutral atomic hydrogen column on the line-of-sight towards 1H 0323+342 is truly this much higher than found by D&L90. Whilst it is known that there are small-scale (∼1–3 arcsec), low-column-density structures which may have been unseen or unresolved by H I 21 cm surveys (Ben Bekhti et al. 2009), we are unaware of such clumps having been detected with column densities as high as implied by our fits ($N_{\rm H} > 10^{20}$ cm^{-2}). If such a neutral absorber were in the Milky Way, we would also expect to see additional reddening in our optical/UV data. However, we find no evidence of additional reddening in our optical/UV data. We measured the equivalent width (EW) of the Na I D absorption line in our Keck spectrum of 2016 February to be EW = 0.891 Å assuming its profile to be similar as that of the broad H β emission line. Using this measurement, we obtain an estimate of the extinction $A_V = 0.483^{+0.098}_{-0.081}$ using the $E(B-V)$-EW(Na I D) relation of Poznanski, Prochaska & Bloom (2012) and assuming the typical Milky Way $R_V = 3.1$. This value is slightly lower than the $A_V = 0.706$ we derived from the literature value of the Galactic H I column.

If the absorber were intrinsic to the AGN, it is possible that there was some occultation of the compact X-ray source but not the more extended optical/UV emission (e.g. Risaliti 2007; Zhang, Yu & Lu 2017). We modelled the *XMM–Newton* EPIC spectra with Galactic plus intrinsic columns. For the intrinsic column we tried both neutral (ZPHABS) and partially-ionized (ZXIPCF) models. The neutral, intrinsic column improves the fit by $\Delta\chi^2 = 104$ for one additional free parameter (a lesser improvement than the additional Galactic column) and we find $N_{\rm H}^{\rm int} = (8 \pm 1) \times 10^{20}$ cm^{-2}. With the ZXIPCF model we obtain a very low ξ value, indicating weakly ionized material, and a high column $N_{\rm H}^{\rm int} = (2 \pm 1) \times 10^{21}$ cm^{-2}. The improvement in the fit is only $\Delta\chi^2 = 11$ for three additional free parameters and this additional ionized intrinsic absorber did not correct the shape of the deabsorbed spectra.

Despite extensive modelling, we have been unable to find a physically plausible model with a column density fixed at the D&L90 value which both reduces the residuals and also gives a corrected shape of the deabsorbed soft spectrum that fits the UV data. We adopted the increased neutral Galactic column as being the simplest model solution which improved our fits and the shape on the intrinsic spectrum.

As we showed in Section 4.1.1, this allows us to fit an energy-conserving accretion disc model which reproduces the optical/UV to hard X-ray data and returns parameters typical of a NLS1. Our jet models would not be substantially changed if we had proceeded with an X-ray spectrum deabsorbed through the D&L90 column density value.

This paper has been typeset from a TEX/LATEX file prepared by the author.